

# Quantum delocalization directs antenna absorption to photosynthetic reaction centers

Felipe Caycedo-Soler<sup>1\*</sup>, Christopher A Schroeder<sup>1,3\*</sup>, Caroline Autenrieth<sup>2</sup>, Robin Ghosh<sup>2</sup>, Susana F Huelga<sup>1</sup>, and Martin B Plenio<sup>1</sup>

<sup>1</sup> *Institute of Theoretical Physics, University of Ulm, Albert-Einstein-Allee 11, D - 89069 Ulm, Germany*

<sup>2</sup> *Department of Bioenergetics, Institute of Biomaterials and Biomolecular Systems, University of Stuttgart, Pfaffenwaldring 57, D - 70569 Stuttgart, Germany*

<sup>3</sup> *Joint Quantum Institute, Department of Physics, University of Maryland and National Institute of Standards and Technology, College Park, MD 20742, USA and*

*\* These authors contributed equally to this work.*

(Dated: April 23, 2015)

The early steps of photosynthesis involve the excitation of reaction centres (RCs) and light-harvesting (LH) units by light. Historically, the electronic coherence across RCs and LH units has been consistently neglected as it does not play a significant role during the relatively slow energy transfer steps of the primary process. Here, we turn our attention to the initial absorption process, which occurs on much shorter timescales. We demonstrate that spatially extended but short-lived excitonic delocalization across RC-LH units plays a relevant role in general photosynthetic systems, as it causes a redistribution of direct absorption towards the charge separation unit. Using the complete core complex of *Rhodospirillum rubrum*, we verify experimentally an 80% increase in the direct optical absorption of the RC *in situ* as compared to isolated RCs. Numerical calculations reveal that similar enhancements can be expected for a wide variety of photosynthetic units in both plant and bacterial systems, suggesting that this mechanism is conserved across species and providing a clear new design principle for light-harvesting nanostructures

Photosynthesis – the conversion of sunlight to chemical energy – is fundamental for supporting life on our planet. Despite its importance, the physical principles that underpin the primary steps of photosynthesis, from photon absorption to electronic charge separation, remain to be understood in full. Excitonic dynamics between tightly-packed pigments, such as within the RC or within the LH units, has been recognized to be of considerable importance for characterizing their individual optical responses and for determining the associated timescales for excitation energy transfer steps<sup>1–6</sup>. For instance, the classical theory of resonance energy transfer between moderately coupled electronic excitations was originally formulated for transport amongst single pigments<sup>7</sup>, and has subsequently required considerable modification for the treatment of excitonic delocalization among several pigments. The modified theory<sup>1</sup>, allows the estimation of energy transfer rates among RC pigments or between LH-bound pigments that belong to the LH units<sup>5</sup> which are in good agreement with the experimental observations. More recently, the study of coherent effects in these biologically relevant systems has increasingly attracted attention due to the observation of long-lasting oscillatory signals measured with time-resolved techniques<sup>8–13</sup> which have driven a wave of theoretical work able to successfully explained these observations<sup>14–25</sup>. These studies have nevertheless confirmed that, even when assuming the electronic coherence between RC and LH units to survive hundreds of femtoseconds, its effect on energy transfer processes between LH and RC, which take place on time scales of tens of picoseconds, is minor<sup>25</sup>. As a consequence, quantum mechanical excitonic delocalization across RC and LH units has so far been consistently ignored. However, we will show that for processes that are taking place on much shorter timescales than energy transfer, excitonic delocalisation among RC and

LH pigments may become relevant.

*The principles of directed absorption* The fundamental principle that motivates both theory and experiment in this work is illustrated in Fig. 1A. Light absorption in photosynthetic complexes occurs predominantly at LH antenna complexes, composed of many pigments, followed by excitation energy transfer to the RC, containing far fewer pigments. The process of photon absorption is described by the absorption spectrum, which quantifies the probability of exciting specific transitions and ultimately, contains signatures of the excitons in an absorbing unit at early times. The excitonic delocalization across RC and LH pigments exists for times determined by the decoherence processes ( $\sim 100$  fs) which are much longer than the few optical cycles ( $\sim 10$  fs) required to imprint its effects on the absorption spectrum. Consequently, even for the case in which excitonic energy transfer (EET) is well-described as a classical transport process, quantum mechanical delocalization of excitons across the entire complex, antenna and RC (see l.h.s. of Fig. 1A), must be accounted for in an accurate description of the absorption process. After a few hundred femtoseconds, environment-induced dephasing will degrade excitonic coherence (see r.h.s. of Fig. 1A) and the subsequent EET can be accurately described by incoherent classical hopping<sup>25</sup>. We will show that even if EET is incoherent, the initial quantum mechanical delocalization in the absorption process can lead, remarkably, to a significant redistribution of absorption intensity from antenna to the RC, thereby increasing the proportion of excitation which produces charge separation without the requirement of further transfer steps.

Our model system for exemplifying this mechanism theoretically and verifying it experimentally is the core complex of the purple bacterium *R. rubrum*<sup>26</sup>. This organism is a freshwater bacterium, which is found in shallow, turbid ponds un-

der conditions of low light intensity and low oxygen tension. Under these conditions the overall light intensity reaching the purple bacterial population at about 2 m depth is extremely low, as indicated by recent *in situ* spectral measurements<sup>27</sup>. We estimate that the incident light intensities could be as low as 60 photons.nm<sup>-2</sup>.ms<sup>-1</sup>, which may be severely limiting, considering that the time for one turnover of photoinduced cyclic electron transport is about 1 ms<sup>28</sup>. Thus, *R. rubrum* is an interesting organism for discovering design principles which have arisen as a response to the strong evolutionary pressure occurring under these low light conditions.

The core complex possesses a photosynthetic RC, containing a “special pair” (*P*) of bacteriochlorophyll (BChl) molecules which mediate the primary process of light-induced charge separation, surrounded by an LH1 complex containing 32 BChls arranged in a protein with ring-like geometry around the RC (Fig. 1A). The absorption spectrum  $A(\lambda)$  of the *P* pigments peaks around 870 nm, whereas the LH1 exhibits a single absorption band at 880 nm, denoted the P870 band and B880 band, respectively (see Fig. 1B and Supplementary Information for spectra). The single LH1 band arises due to the circular arrangement of the 32 BChls with the  $Q_y$  transition dipoles lying almost tangentially to the LH1 circumference. The spectral bands of the *P* pigments or LH1 correspond to transitions from the electronic ground state to the excited states  $|P870\rangle$  and  $|B880\rangle$ , and their strengths are determined by the effective dipole moments  $\vec{D}_{P870}$  and  $\vec{D}_{B880}$ , respectively, according to  $A(\lambda) \propto |\vec{D}_\lambda|^2$  (see Supplementary Information).

## RESULTS

One tantalizing and experimentally verifiable consequence of our full Monte-Carlo numerical simulations is a significant increase of the direct absorption of the *P* pigments when in the core complex (Fig. 1B). The full numerical simulations take into account all the pigments which compose the core complex, subject to variations in energies and coupling strengths induced by the highly dynamical protein scaffold (details in the Supplementary Information). However, the key result can be understood by a simple model with two effective excited states  $|P870\rangle$  and  $|B880\rangle$  coherently coupled with strength  $V$  through the Coulomb interaction between their transition dipoles, as described by a Hamiltonian of the form

$$\mathcal{H} = \Delta E |P870\rangle \langle P870| + V(|P870\rangle \langle B880| + |B880\rangle \langle P870|), \quad (1)$$

where  $\Delta E = E_{P870} - E_{B880} > 0$  is the inter-band energy difference between the two bands. The eigenstates  $|\alpha\rangle$  of the system Hamiltonian in Eq. (1) are delocalised across both the RC and the LH1 and lead to dipole moments  $\vec{D}'_\alpha$ , which become linear combinations of  $\vec{D}_{P870}$  and  $\vec{D}_{B880}$ . To lowest order in  $(V/\Delta E)$ , valid when  $V \ll \Delta E$ , (full expressions in Supplementary Information) this redistribution of dipole strength can be written

$$|\vec{D}'_{P870}|^2 = |\vec{D}_{P870}|^2 + 2 \vec{D}_{P870} \cdot \vec{D}_{B880} \left( \frac{V}{\Delta E} \right) + \dots \quad (2)$$

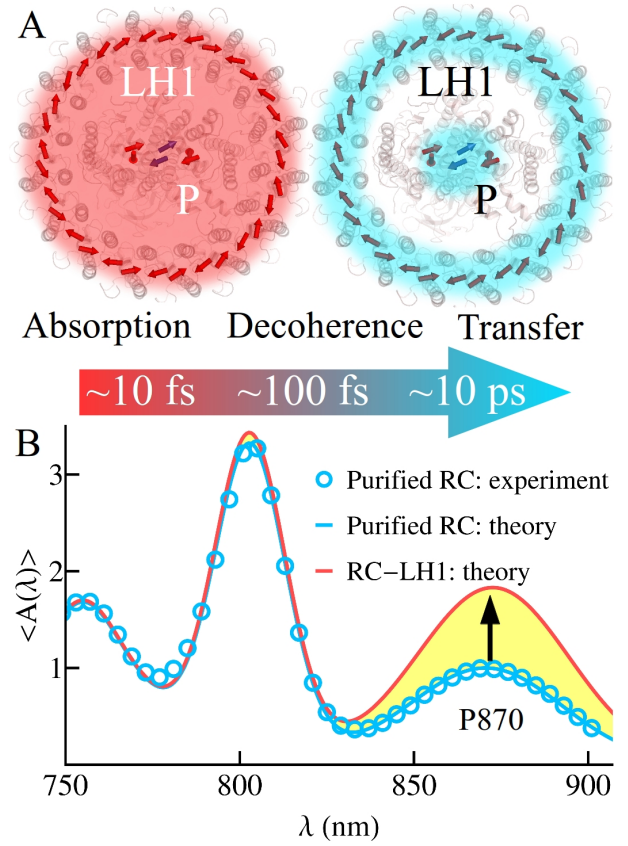


**Figure 1. Evolution of coherence and the relevance of differentiated time scales.** (A) Schematic representation of the *R. rubrum* RC-LH1 bacteriochlorophyll (BChl) pigments. The positions of the LH1 and RC BChls have been obtained from a molecular model (see Supplementary Information). After a few hundred femtoseconds, environment-induced dephasing will degrade the quantum mechanical delocalization between the antenna and the RC (red shading), and transforms into a statistical mixture of populations residing either on the antenna or the RC (blue shading), meaning that absorption is coherent while transfer is not. (B) Experimental and theoretical absorption spectrum of the *R. rubrum* RC. Extended delocalization across the RC-LH1 leads to an 80 % increase in absorption intensity of the P870 band, as illustrated by the area (yellow) between the spectra for the core complex and for purified RC.

The coherent nature of the coupling is manifested in two measurable optical signatures: spectral shifts and absorption intensity redistributions, which scale as  $(V/\Delta E)^2$  and  $V/\Delta E$ , respectively, to lowest order. Hence, in the core complex, where coupling among RC and LH1 satisfies  $V \ll \Delta E$ , excitonic coupling may lead to a measurable absorption intensity redistribution while leaving spectral positions almost unaffected due to the quadratic dependence on  $(V/\Delta E)$ .

According to equation (2), absorption of the P870 band is enhanced when the ratio  $(\vec{D}_{P870} \cdot \vec{D}_{B880})(V/\Delta E)$  is positive. Under these conditions, the absorption of the B880 band decreases in equal measure such that the total absorption intensity remains constant. The geometrical details of the core complex imply that  $(\vec{D}_{P870} \cdot \vec{D}_{B880})V > 0$ , a direct consequence of the almost tangential arrangement of LH1 BChl transition

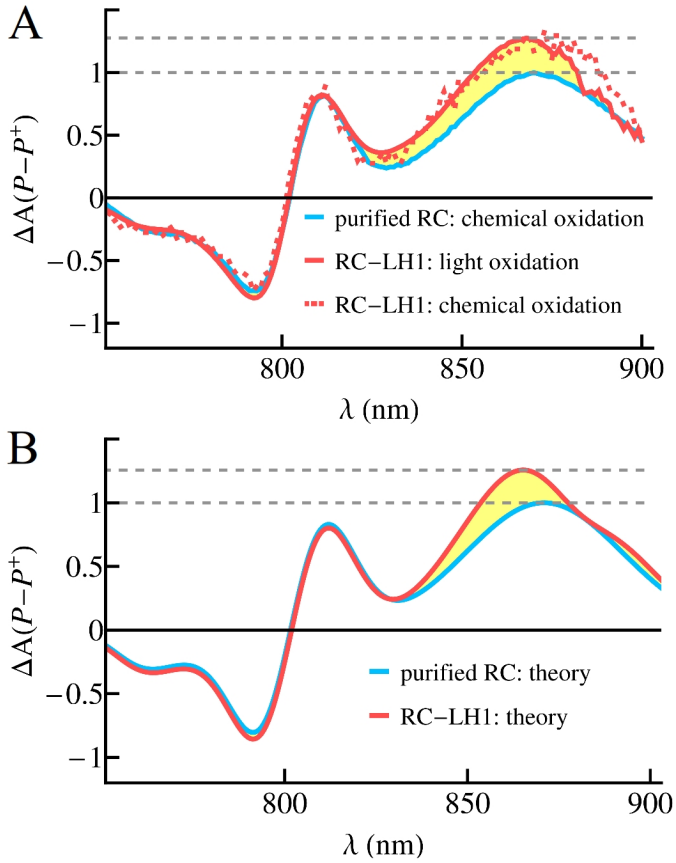


Figure 2. **Comparison of the absorption redistribution between experiment and theory.** (A) Experimentally determined difference spectra of pigment-protein complexes under different oxidation conditions. (B) Theoretical prediction of redox difference spectra shown in (A). Yellow shading indicates a redistribution of absorption which results from increased P870 absorption and a concomitant decrease in that of the B880.

dipoles<sup>29,30</sup>. Therefore,  $\Delta E > 0$  provides an energy landscape that *inhibits* energy transfer funneling to the RC, enhancing P870 band absorption at the expense of *slowing* the LH1  $\rightarrow$  P transfer step.

**Experimental confirmation of directed absorption** The experimental confirmation of the predicted enhancement of the P870 absorption due to quantum excitonic delocalization is complicated by the fact that the P870 absorption spectrum overlaps with the much stronger optical response of the LH1 B880 band. We carried out two independent procedures for the oxidation reaction,  $P \rightarrow P^+$ , namely, optical excitation or stoichiometric addition— in the dark— of the oxidising agent potassium ferricyanide as explained in detail in the Supplementary Information. The oxidation reaction moves the P870 resonance to 1260 nm, far into the infrared region, and therefore effectively suppresses the resonant coherent interaction between P and LH1 pigments<sup>31</sup>. Subtracting core complex spectra of oxidised  $P^+$  from those of neutral P filters out the overwhelming B880 component and highlights the changes in the absorbing bands due to the coherent interaction V. With both procedures we observed difference spectra from

core complexes and purified RCs (Fig. 2A) which are in good agreement with theoretical calculations (Fig. 2B), and consistent with an 80 % increase in P870 absorption in the former over the latter (Fig. 1B).

The enhanced absorption of the P870 band leads to the excitation of a state that is partially delocalised over P and LH1 pigments, so it is not immediately clear that increased absorption at 870 nm implies the increased excitation of the P-pigments, which is desirable as it places excitations directly where charge separation takes place. Even though the BChls have several optical transitions besides the  $Q_y$  transition, under physiological conditions, the  $Q_y$  transition(s) is the most relevant in *R. rubrum*. Indeed, recently published complete spectra from different water depths in oceans and lakes<sup>27</sup> showed that in coastal waters and peat lakes blue light is absent, and that the spectra of these ecosystems are dominated by red and near-IR light. As such, under incoherent broadband illumination covering the entire near-IR spectral range, the prominent excitation concerns the  $Q_y$  transitions. Thus, under physiological conditions, the excitation population of the special pair,  $P_P(0)$ , is determined by the absorption from the  $Q_y$  transitions, accounted for by a state  $\rho(0) \propto \sum_{\alpha} |\vec{D}'_{\alpha}|^2 |\alpha\rangle \langle \alpha|$ . The requirement that many harvesting pigments should surround fewer charge separation pigments in order to increase the excitation of charge separation pigments, is illustrated by an analytical expression for  $P_P(0) = \text{Tr} \{ \rho(0) |P\rangle \langle P| \}$  in the absence of protein-induced inhomogeneities

$$P_P(0) = \frac{1}{M+N} \left( N + \sqrt{2MN} \left( \frac{V}{\Delta E} \right) + (M-2N) \left( \frac{V}{\Delta E} \right)^2 + \dots \right) \quad (3)$$

where  $M$  represents the number of excitonically-coupled harvesting units encircling the  $N$  pigments that initiate charge separation in the RC (see Supplementary Information). In the particular case of the core complex these correspond to  $M = 32$  pigments for the LH1 and  $N = 2$  pigments for the special pair. Full numerical simulations of the complete core complex result in a two-fold average increase of population  $P_P(0)$  due to extended delocalization over antenna pigments, and it provides the initial condition for dynamical simulations of EET (see Fig. 3). The probability of charge separation,  $P_{P^+}(t)$ , increases as extended delocalization focuses the excitation into the special pair, allowing the excitation to avoid the slow transfer step from LH1 to RC. This increase in charge separation provides a quantitative link between a coherent quantum effect and enhanced functionality.

It is important to note that the physiological environment of light-harvesting complexes is highly disordered and dynamic, leading to variations in the excitonic energy splitting  $\Delta E$ . Upon averaging the complete expressions that lead to perturbative equations (2) and (3) over appropriate distributions (see Supplementary Information), Figure 4 shows that excitation population is redistributed from antenna to P pigments for all realistic levels of disorder. Moreover, a maximum occurs for intermediate values of disorder, equal to half the excitonic energy splitting,  $\Delta E/2$ . Remarkably, the parameters which are consistent with pump-probe studies in RCs<sup>1</sup> and reproduce our experimental dark-minus-light spectra (see

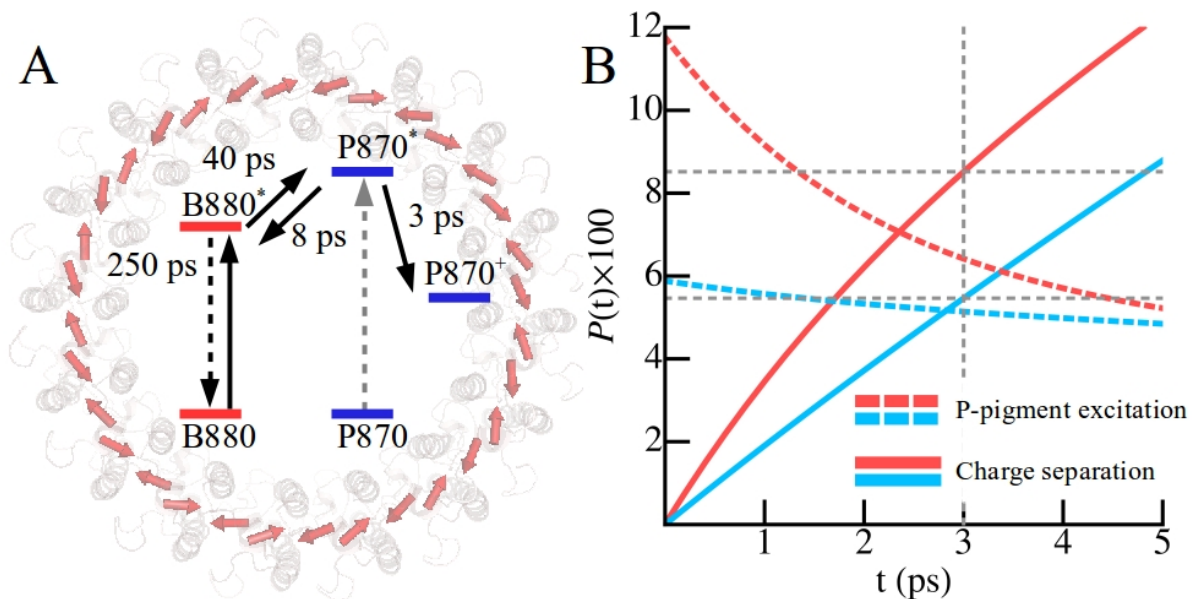


**Figure 3. Absorption redistribution enhances charge separation.** (A) Transport dynamics in *R. rubrum* can be accurately modeled using classical rate equations (see Supplementary Information). (B) Both the initial excitation of *P*-pigments ( $P_P(t)$  (dashed lines)) and the resulting process of charge separation,  $P_{P^+}(t)$  (solid lines), are increased when absorption is delocalized across the core complex (red) as compared to absorption occurring either on the RC or LH1 (blue). The enhancement is relevant on a timescale comparable to the charge separation process (3 ps, grey line), well before EET from LH1 to RC takes place ( $\sim 40$  ps). The initial excitation of *P*-pigments increases from 2/34 to 4/34 (an increase of 100%), and results in a  $\sim 1\%$  increase in photosynthetic efficiency at long times.

Supplementary Information) optimize the population redistribution to the *P* pigments. Accordingly, neglecting disorder underestimates the 80% enhancement in the P870 direct optical absorption, presented in Figure 1, due to this non-trivial enhancement arising from protein-induced inhomogeneities.

**Generality of directed absorption in nature** The redirection of excitation towards the special pair due to extended quantum delocalization can be generalized to other organisms by theoretical analysis. When environmentally-induced disorder is included, numerical simulations predict similar redistributions of excitation population in other purple bacteria species ( $N = 2, M = 28 - 32$ ) which show structural deviations from a closed circular ring. In photosystem 1 (PS1) (see Fig. 4) of higher plants ( $N = 2, M = 83$ ), our analysis indicates a 14 % increase of the excitation population of the *P*-pigments due to excitonic delocalization over antenna pigments. For the photosystem 2 (PS2) we predict a 12 % increase in *P*-excitation for both the monomer ( $N = 2, M = 35$ ) and natural dimeric structure ( $N = 4, M = 70$ ) (see Supplementary Information for further details).

## DISCUSSION

**Natural optimization of *R. rubrum* core complex** It is interesting to examine the extent to which the design of the LH1-RC unit is optimized with respect to the population redistribution due to excitonic delocalization. Figure 4 analyses the situation of ring-like LH units and shows that the optimal population redistribution occurs when the RC contains a

small number of pigments,  $N$ , able to initiate charge separation, while the LH unit contains a few tens of pigments,  $M$ , i.e.  $N \ll M$ , as expected from Eq. (3). A greater number  $M$  of harvesting pigments naturally increases the distance of the LH to the RC pigments, reducing the coherent coupling,  $V$ , and therefore weakening the population redistribution, also illustrated by Eq. (3). Photosynthetic complexes typically contain  $N = 2$  pigments which promote charge separation. In this case, the maximal enhancement for direct excitation is achieved with  $M \sim 20$  pigments in the LH unit, closely resembling the LH1 structure.

**Design principles: focusing absorption in artificial devices** A quantitative understanding of light harvesting in the LH1-RC complex illuminates clear design principles for devices engineered to direct light collection. These principles could prevent photobleaching and lengthen the lifetime of harvesting devices by directing absorption to stable target pigments, in addition to increasing the efficiency from photon absorption to charge separation. By tuning the resonance condition  $\Delta E$  in a ring-like geometry, a 400% increase in the absorption of a few target pigments can be achieved. Moreover, in devices where dissipation is fast ( $\sim 15$  ps as opposed to 250 ps in LH1<sup>32</sup>), these configurations will lead to a 54% gain in achieving charge separation following photon absorption (see Supplementary Information).

In conclusion, theoretical considerations have led us to identify a new design principle which exploits quantum delocalization to redirect light absorption to the RC in several photosynthetic systems. Given the generality of the design principle described here, it is tempting to equate this princi-



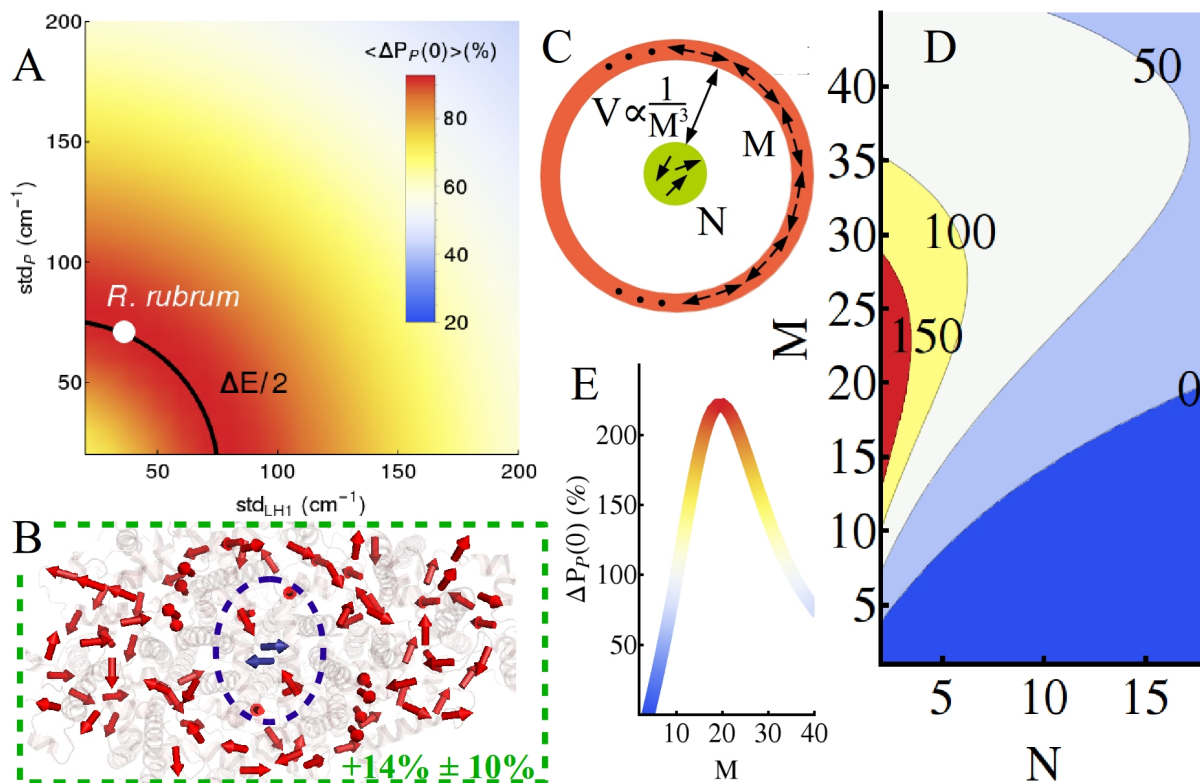


Figure 4. **Inhomogeneous broadening and clustering of LH and P pigments as design principles for optimal performance.** Excitation population is redistributed from antenna to *P* pigments (A) for levels of disorder up to the full spectral linewidth ( $\text{std} \sim 200\text{--}300 \text{ cm}^{-1}$ ). The redistribution is, remarkably, noise-assisted, as the optimal redistribution occurs in *R. rubrum* for intermediate levels of disorder ( $\sqrt{\text{std}_P^2 + \text{std}_{LH1}^2} = \Delta E/2 = 65 \text{ cm}^{-1}$ ). PS1 (B) and PS2 (see Supplementary Information) exhibit clustering of many LH pigments around fewer RC pigments (bound in dark blue). The excitation population of the *P*-pigments (dark blue arrows) *increases* when extended delocalization over all antenna pigments (bound in green) is taken into account. Error bound corresponds to the width of distribution when averaging over the effects of environmental disorder. Using a simplified model for a general circular aggregate (C), the percent increase of the initial excitation of the *P*-pigments is calculated (D) as a function of the number *N* of *P*-pigments and number *M* of LH pigments, and (E) as a function of the number *M* of LH pigments fixing *N* = 2. The enhancement of direct *P*-pigment excitation requires  $N \ll M$  and is maximized for  $M \sim 20$ .

ple with increased evolutionary fitness of certain biological systems<sup>33</sup>. We have verified this principle experimentally in the core complexes of *R. rubrum*, and our detailed theoretical analysis illuminates clear guidelines for the design of light-harvesting devices that direct photon absorption. This new quantum design principle provides a quantitative link between structure and function, broadening our understanding of the role of quantum mechanics in light harvesting.

We acknowledge discussions with Fedor Jelezko, Jaemin Lim and Shai Machnes. The work was supported by the EU Synergy Grant BioQ, the EU STREP PAPETS, the SFB TRR/21 and an Alexander von Humboldt Professorship. Additional support was provided by the National Science Foundation through PFC@JQI and the National Science Foundation Graduate

## REFERENCES

- <sup>1</sup>X. J. Jordanides, G. D. Scholes, and G. R. Fleming, "The mechanism of energy transfer in the bacterial photosynthetic reaction center," *J. Phys. Chem. B* **105**, 1652–1669 (2001).
- <sup>2</sup>J. Adolphs and T. Renger, "How proteins trigger excitation energy transfer in the FMO complex of green sulfur bacteria," *Biophys. J.* **91**, 2778–2797 (2006).
- <sup>3</sup>S. Georgakopoulou, R. van Grondelle, and G. van der Zwan, "Explaining the visible and near-infrared circular dichroism spectra of light-harvesting 1 complexes from purple bacteria: a modeling study," *J. Phys. Chem. B* **110**, 3344–3353 (2006).
- <sup>4</sup>K. Timpmann, G. Trinkunas, P. Qian, and C. N. Hunter, "Excitons in core LH1 antenna complexes of photosynthetic bacteria: evidence for strong resonant coupling and off-diagonal disorder," *Chem. Phys. Lett.* **414**, 359–363 (2005).
- <sup>5</sup>Y. C. Cheng and R. J. Silbey, "Coherence in the B800 ring of purple bacteria LH2," *Phys. Rev. Lett.* **96**, 028103 (2006).
- <sup>6</sup>A. Olaya-Castro, C. F. Lee, F. Fassioli Olsen, and N. F. Johnson, "Efficiency of energy transfer in a light-harvesting system under quantum coherence," *Phys. Rev. B* **78**, 085115 (2008).
- <sup>7</sup>T. Förster, *Delocalized excitation and excitation transfer*, edited by M.-M. Beyerle (Academic Press, New York, 1965) pp. 93–137.
- <sup>8</sup>G. S. Engel, T. R. Calhoun, E. L. Read, T.-K. Ahn, T. Mancal, Y. C. Cheng, R. E. Blankenship, and G. R. Fleming, "Evidence for wavelike energy transfer through quantum coherence in photosynthetic systems," *Nature* **446**, 782–786 (2007).
- <sup>9</sup>E. Collini, C. Y. Wong, K. E. Wilk, P. M. G. Curmi, P. Brumer, and G. D. Scholes, "Coherently wired light-harvesting in photosynthetic marine algae

- at ambient temperature,” *Nature* **463**, 644–647 (2010).
- <sup>10</sup>G. Panitchayangkoon, D. Hayes, K. A. Fransted, J. R. Caram, E. Harel, J. Wen, R. E. Blankenship, and G. S. Engel, “Long-lived quantum coherence in photosynthetic complexes at physiological temperature,” *Proc. Natl. Acad. Sci. USA* **107**, 12766–12770 (2010).
  - <sup>11</sup>R. Hildner, D. Brinks, J. B. Nieder, R. J. Cogdell, and N. F. Van Hulst, “Quantum coherent energy transfer over varying pathways in single light-harvesting complexes,” *Science* **340**, 1448–1451 (2013).
  - <sup>12</sup>E. Romero, R. Augulis, V. I. Novoderezhkin, M. Ferretti, J. Thieme, D. Zigmantas, and R. van Grondelle, “Quantum coherence in photosynthesis for efficient solar-energy conversion,” *Nature Phys.* **10**, 676–682 (2014).
  - <sup>13</sup>F. D. Fuller, J. Pan, A. Gelzinis, V. Butkus, S. S. Senlik, D. E. Wilcox, C. F. Yocum, L. Valkunas, D. Abramavicius, and J. P. Ogilvie, “Vibronic coherence in oxygenic photosynthesis,” *Nat. Chem.* **6**, 706–711 (2014).
  - <sup>14</sup>V. Tiwari, W. K. Peters, and D. M. Jonas, “Electronic resonance with anti-correlated pigment vibrations drives photosynthetic energy transfer outside the adiabatic framework,” *PNAS* **110**, 1203–1208 (2013).
  - <sup>15</sup>M. B. Plenio, J. Almeida, and S. F. Huelga, “Origin of long-lived oscillations in 2d-spectra of a quantum vibronic model: electronic versus vibrational coherence,” *J. Chem. Phys.* **139**, 235102 (2013).
  - <sup>16</sup>F. Caycedo-Soler, A. W. Chin, J. Almeida, S. F. Huelga, and M. B. Plenio, “The nature of the low-energy band of the Fenna-Matthews-Olson complex: vibronic signatures,” *J. Chem. Phys.* **136**, 155102 (2012).
  - <sup>17</sup>N. Christensson, H. F. Kauffmann, T. Pullerits, and T. Mančal, “Origin of long-lived coherences in light-harvesting complexes,” *J. Phys. Chem. B* **116**, 7449–7454 (2012).
  - <sup>18</sup>M. Mohseni, P. Rebentrost, S. Lloyd, and A. Aspuru-Guzik, “Environment-assisted quantum walks in photosynthetic energy transfer,” *J. Chem. Phys.* **129**, 174106 (2008).
  - <sup>19</sup>M. B. Plenio and S. F. Huelga, “Dephasing assisted transport: quantum networks and biomolecules,” *New J. Phys.* **10**, 113019 (2008).
  - <sup>20</sup>A. Kolli, E. J. O’Reilly, G. D. Scholes, and A. Olaya-Castro, “The fundamental role of quantized vibrations in coherent light-harvesting by cryptophyte algae,” *J. Chem. Phys.* **137**, 174109 (2012).
  - <sup>21</sup>A. W. Chin, J. Prior, R. Rosenbach, F. Caycedo-Soler, S. F. Huelga, and M. B. Plenio, “The role of non-equilibrium vibrational structures in electronic coherence and recoherence in pigment protein complexes,” *Nature Phys.* **9**, 113–118 (2013).
  - <sup>22</sup>S. F. Huelga and M. B. Plenio, “Vibrations, quanta and biology,” *Contemporary Physics* **54**, 181–207 (2013).
  - <sup>23</sup>A. Chin, A. Datta, F. Carusso, S. F. Huelga, and M. B. Plenio, “Noise-assisted energy transfer in quantum networks and light-harvesting complexes,” *New J. Physics* **12**, 065002 (2010).
  - <sup>24</sup>J. Womick and A. Moran, “Vibronic enhancement of exciton sizes and energy transport in photosynthetic complexes,” *J. Phys. Chem. B* **115**, 1347–1356 (2011).
  - <sup>25</sup>J. Strümpfer and K. Schulten, “Excited state dynamics in photosynthetic reaction center and light harvesting complex 1,” *J. Chem. Phys.* **137**, 065101 (2012).
  - <sup>26</sup>H. Stahlberg, J. Dubochet, H. Vogel, and R. Ghosh, “Are the light-harvesting I complexes from *Rhodospirillum rubrum* arranged around the reaction centre in a square geometry?” *J. Mol. Biol.* **282**, 819–831 (1998).
  - <sup>27</sup>M. Stomp, J. Huisman, L. J. Stal, and H. C. P. Matthijs, “Colorful niches of phototrophic microorganisms shaped by vibrations of the water molecule,” *ISME J.* **1**, 271–282 (2007).
  - <sup>28</sup>S. Osváth and P. Maróti, “Coupling of cytochrome and quinone turnovers in the photocycle of reaction centers from the photosynthetic bacterium *rhodospirillum rubrum*,” *Biophys. Journ.* **73**, 972–982 (1997).
  - <sup>29</sup>S. Karrasch, P. A. Bullough, and R. Ghosh, “The 8.5 Å projection map of the light-harvesting complex 1 from *Rhodospirillum rubrum* reveals a ring composed of 16 subunits,” *EMBO J.* **14**, 631–638 (1995).
  - <sup>30</sup>A. W. Roszak, T. D. Howard, J. Southall, A. T. Gardiner, C. J. Law, N. W. Isaacs, and R. J. Cogdell, “Crystal structure of the RC-LHI core complex from *Rhodospseudomonas palustris*,” *Science* **302**, 1969–1972 (2003).
  - <sup>31</sup>A. J. Jackson, S. Lin, A. K. W. Taguchi, J. C. Williams, J. P. Allen, and N. W. Woodbury, “Energy transfer in rhodospirillum rubrum reaction centers with the initial electron donor oxidised or missing,” *J. Phys. Chem. B* **101**, 5747–5754 (1997).
  - <sup>32</sup>A. Freiberg and K. Timpmann, “Picosecond fluorescence spectroscopy of light-harvesting antenna complexes from *Rhodospirillum rubrum* in the 300–4 K temperature range. Comparison with the data on chromatophores,” *J. Photochem. Photobiol. B; Biol.* **15**, 151–158 (1992).
  - <sup>33</sup>We use the term evolutionary fitness here to describe an adaptive property which may help an organism to survive under given environmental conditions (e.g. low light intensity), and not in its usual context of increased growth rate, which may be determined by other factors not under consideration here

## Appendix A: Materials and Methods

### 1. LH1 structure and Hamiltonian

In this study we have employed a model of the *R. rubrum* LH1 where 32 BChl molecules, bound to 16  $\alpha$  and  $\beta$  polypeptides as  $\alpha\beta(\text{BChl})_2$  subunits, are arranged in a ring-like geometry with  $C_{16}$  symmetry, see Fig. S1. The model was constructed in the group of one of the present authors (R. Ghosh<sup>1</sup>) in a collaboration with the group of Klaus Schulten (Beckmann Institute, University of Illinois, Urbana-Champaign) in 2002, and was based upon both extensive biochemical and biophysical data, low-resolution projection structures obtained using cryoelectron microscopy (cryoEM) of 2D crystals<sup>2,29</sup>, and homology modelling to the known X-ray structures of the LH2 complexes from *Rhodospirillum molischianum*<sup>3</sup> and *Rhodopseudomonas acidophila*<sup>4</sup> as well as a further homology model of the LH1 structure from *Rhodobacter sphaeroides*<sup>5</sup>. The data from this model, as well as that for the complete *R. rubrum* photosynthetic unit (PSU) (containing the RC) has been used subsequently for biophysical studies of this complex<sup>6-8</sup>.

The  $C_{16}$  symmetry naturally arises from the energy minimization procedure needed to construct the model, and is one of the controversial aspects since it contradicts AFM and cryoEM data obtained for LH1 complexes of other organisms<sup>2,9</sup>. However, fluorescence polarization data obtained from both purified *R. rubrum* LH1 and LH1-RC complexes, respectively, reconstituted and diluted into bilayer membranes<sup>6,7</sup>, have consistently yielded results consistent with  $C_{16}$  symmetry, so we feel justified to employ this assumption for the calculations made here. Very recently, the X-ray structure of a thermostable LH1-RC complex from *Thermochromatium tepidum* at near-atomic resolution of 3.0 Å has been published<sup>10</sup>. This LH1-RC complex is also comprised of 16  $\alpha\beta(\text{BChl})_2$  units which form a closed ring, and thus strongly resembles the *R. rubrum* PSU model employed here. However, the *T. tepidum* complex also shows overable ellipticity. Nevertheless, the distances and geometries of the BChl pigments do not differ strongly from our *R. rubrum* model. Furthermore, the crystals were grown in detergent, which may have a destabilizing effect upon the geometry of the LH1-RC complex.

In this study, we have employed the assumption of  $C_{16}$  symmetry for the structure of the LH1. Its pigments are identified by indices  $(m, \zeta)$ , where  $m \in \{-M/4 + 1, \dots, M/4\}$  labels the (dimerized) unit cell ( $M = 32$ ), and  $\zeta \in \{1, 2\}$  labels the pigment within the  $\alpha\beta$  heterodimer. Low energy spectral features can be characterized using the  $Q_y$  optically-induced transition dipole moments of the BChl, which lie along a line joining the nitrogens of unreduced pyrrole rings I and III<sup>11</sup>. A general parameterization of the LH1 BChl positions,  $\vec{r}_{m,\zeta}$ , and the

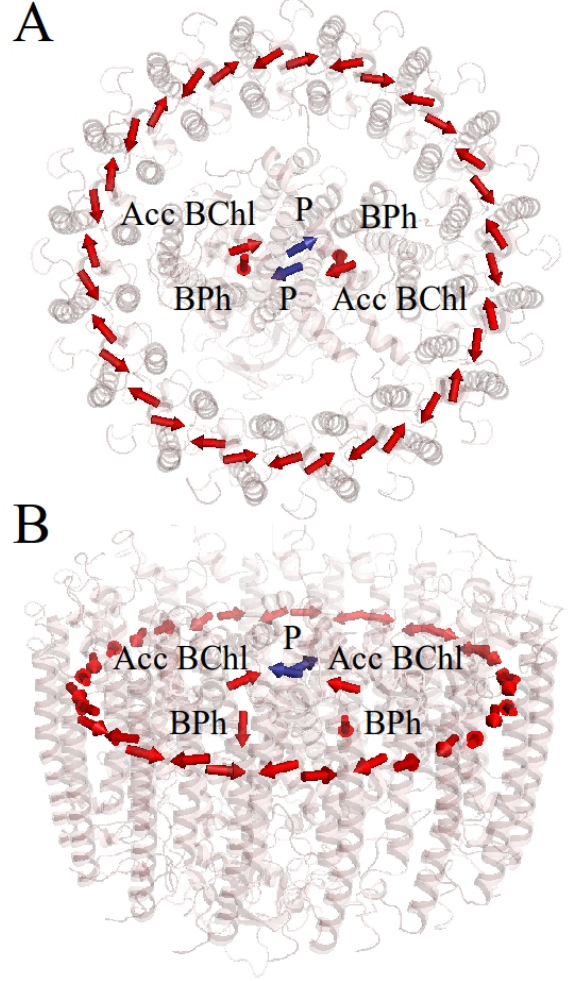


Figure 5. (A), (B) The position of the BChl and bacteriopheophytin pigments in the atomic model of the *R. rubrum* LH1-RC complex used here. The orientations of the  $Q_y$  transition moments of the pigments are shown with arrows. The special pair ( $P$ ), accessory BChls ( $B_L$  and  $B_M$ ) and bacteriopheophytins ( $H_L$  and  $H_M$ ) of the RC are also indicated. The  $\alpha$  and  $\beta$  protein subunits are rendered translucent.

corresponding  $Q_y$  transition dipole moments,  $\vec{d}_{m,\zeta}$ , is:

$$\vec{d}_{m,\zeta} = d \begin{pmatrix} -(-1)^\zeta \sin\left(\frac{4\pi}{M}m + \frac{\gamma}{2}(-1)^\zeta + \Delta\gamma_\zeta\right) \cos\phi_\zeta \\ (-1)^\zeta \cos\left(\frac{4\pi}{M}m + \frac{\gamma}{2}(-1)^\zeta + \Delta\gamma_\zeta\right) \cos\phi_\zeta \\ \sin\phi_\zeta \end{pmatrix}$$

$$\vec{r}_{m,\zeta} = \begin{pmatrix} r_\zeta \cos\left(\frac{4\pi}{M}m + \frac{\gamma}{2}(-1)^\zeta\right) \\ r_\zeta \sin\left(\frac{4\pi}{M}m + \frac{\gamma}{2}(-1)^\zeta\right) \\ (-1)^\zeta z/2 \end{pmatrix}. \quad (\text{A1})$$

An explanation of structural parameters and the values used in the full numerical study are summarized in Table S1. A correspondence between microscopic structure and optical properties is possible by a theoretical analysis using a Hamiltonian

coupling  $Q_y$  transition dipoles. We consider the Hamiltonian:

$$H = \sum_{m,\zeta} \epsilon_{m,\zeta} |m, \zeta\rangle \langle m, \zeta| + \sum_{(m,\zeta) \neq (m',\zeta')} J_{m,\zeta}^{m',\zeta'} |m, \zeta\rangle \langle m', \zeta'| + H.c. \quad (A2)$$

where  $\epsilon_{m,\zeta}$  is the site energy of BChl ( $m, \zeta$ ) and  $J_{m,\zeta}^{m',\zeta'}$  is the interaction energy between pigments ( $m, \zeta$ ) and ( $m', \zeta'$ ). When the details of the charge distribution of excited states are of no importance,  $J_{m,\zeta}^{m',\zeta'}$  can be calculated using the point-dipole approximation:

$$J_{m,\zeta}^{m',\zeta'} = \frac{1}{4\pi\kappa} \left( \frac{\vec{d}_{m,\zeta} \cdot \vec{d}_{m',\zeta'}}{|\Delta\vec{r}_{m,\zeta}^{m',\zeta'}|^3} - \frac{3(\vec{d}_{m,\zeta} \cdot \Delta\vec{r}_{m,\zeta}^{m',\zeta'})(\vec{d}_{m',\zeta'} \cdot \Delta\vec{r}_{m,\zeta}^{m',\zeta'})}{|\Delta\vec{r}_{m,\zeta}^{m',\zeta'}|^5} \right), \quad (A3)$$

where  $\Delta\vec{r}_{m,\zeta}^{m',\zeta'} = \vec{r}_{m,\zeta} - \vec{r}_{m',\zeta'}$  and  $\kappa$  is the relative permittivity. The sub-nanometer distance between neighbouring chromophores implies that the nearest-neighbour couplings depend on the geometry of the electronic wave-function of each chromophore. These couplings can be fitted using fluorescence anisotropy measurements, resulting in  $Q_1 = 600 \text{ cm}^{-1}$  and  $Q_2 = 377 \text{ cm}^{-1}$  for the intra- and inter-dimer couplings, respectively<sup>4</sup>.

Diagonalization of equation A2 leads to excitons  $|\alpha\rangle = \sum_{m,\zeta} c_{m,\zeta}^\alpha |m, \zeta\rangle$ , where  $\alpha$  is a collection of quantum numbers which describe the state. The optical response depends on the dipole moment of the exciton states:

$$\vec{D}_\alpha = \sum_{m,\zeta} c_{m,\zeta}^\alpha \vec{d}_{m,\zeta} \quad (A4)$$

and is calculated by means of the Fermi's Golden Rule-type expression

$$\langle A(\lambda) \rangle = \sum_\alpha |\vec{D}_\alpha|^2 f(\lambda - \lambda_\alpha). \quad (A5)$$

where homogeneous broadening is taken into account with a lineshape function,  $f$ . The brackets correspond to ensemble averages that take into account inhomogeneous broadening over distributions of fluctuations in the site-energies and nearest-neighbour couplings.

## 2. Analytical Results

### a. Dipole Redistribution

The exciton states of circular aggregates are well-known<sup>12</sup>, and modeling the LH1 complex with a  $C_{16}$  symmetry allows simple analytical expressions for noiseless spectral observables. To make these expressions transparent, we consider a simplified model whereby the transition dipoles sit on a two-dimensional ring of radius  $R$ , the BChl are degenerate in energy  $\epsilon$  and share a common dipole moment strength  $d$ , and only nearest-neighbour couplings are taken into account. The

necessary parameters are given in the Supplementary Table S6. The Hamiltonian of equation A2 is best examined in the Fourier basis

$$|k, \zeta\rangle = \frac{1}{\sqrt{M/2}} \sum_m e^{i\frac{4\pi}{M}km} |m, \zeta\rangle \quad (A6)$$

where  $k \in \{-M/4 + 1, \dots, M/4\}$ . In this basis, the states decouple for different values of  $k$

$$\langle k, \zeta | H | k', \zeta' \rangle = L_{\zeta,\zeta'}(k) \delta_{k,k'} \quad (A7)$$

$$L_{\zeta,\zeta'}(k) = \sum_m e^{i\frac{4\pi}{M}km} \langle 0, \zeta | H | m, \zeta' \rangle. \quad (A8)$$

The diagonalisation of the  $2 \times 2$  Hamiltonians restricted to each  $k$ -subspace,  $L(k)$ , is accomplished with the unitary:

$$U(k) = \begin{pmatrix} e^{i\Phi(k)/2} \cos \Theta(k) & e^{i\Phi(k)/2} \sin \Theta(k) \\ -e^{-i\Phi(k)/2} \sin \Theta(k) & e^{-i\Phi(k)/2} \cos \Theta(k) \end{pmatrix} \quad (A9)$$

where  $\Phi(k) = \arg(L_{01}(k))$  and  $\Theta(k) = \frac{1}{2} \arctan \frac{2|L_{01}(k)|}{L_{00}(k) - L_{11}(k)}$  reflect the ‘‘amount of dimerisation’’:  $\Phi(k)$  captures the difference between intra- and inter-dimer coupling, and  $\Theta(k)$  captures the site energy differences.

Considering degenerate dimers and taking into account only nearest neighbour coupling, the matrix  $L$  takes on a particularly simple form:

$$L(k) = \begin{pmatrix} \epsilon & Q_1 + Q_2 e^{i\frac{4\pi}{M}k} \\ Q_1 + Q_2 e^{-i\frac{4\pi}{M}k} & \epsilon \end{pmatrix} \quad (A10)$$

where  $\epsilon$ ,  $Q_1$ ,  $Q_2$  are site energies, and intra-dimer and inter-dimer couplings, respectively. Accordingly:

$$\begin{aligned} \Theta(k) &= \frac{\pi}{4} \\ \Phi(k) &= \arctan \frac{Q_2 \sin \frac{4\pi}{M}k}{Q_1 + Q_2 \cos \frac{4\pi}{M}k}. \end{aligned} \quad (A11)$$

The Hamiltonian is diagonalized by the exciton wavefunctions  $|k, \nu\rangle$ , leading to dipole moments  $\vec{D}_{k,\nu}$  and energies  $E(k, \nu)$ :

$$|k, \nu\rangle = \sum_{m,\zeta} c_{m,\zeta}^{k,\nu} |m, \zeta\rangle = \frac{1}{\sqrt{M/2}} \sum_{m,\zeta} e^{i\frac{4\pi}{M}km} U(k)_{\zeta,\nu} |m, \zeta\rangle \quad (A12)$$

$$\vec{D}_{k,1} = \delta_{k,\pm 1} d \sqrt{M/2} \cos \left( \frac{\Phi(1) + \gamma}{2} \right) \frac{e^{\pm i\Delta\gamma}}{\sqrt{2}} \begin{pmatrix} \mp \frac{i}{\sqrt{2}} \\ \frac{1}{\sqrt{2}} \end{pmatrix} \quad (A13)$$

$$\vec{D}_{k,2} = \delta_{k,\pm 1} d \sqrt{M/2} \sin \left( \frac{\Phi(1) + \gamma}{2} \right) \frac{e^{\pm i\Delta\gamma}}{\sqrt{2}} \begin{pmatrix} \frac{1}{\sqrt{2}} \\ \mp \frac{i}{\sqrt{2}} \end{pmatrix} \quad (A14)$$

$$E(k, \nu) = \epsilon + (-1)^\nu \left( Q_1 + Q_2 \cos \frac{4\pi}{M}k \right), \quad (A15)$$

where  $\gamma$  is the intra-dimer angle and  $\Delta\gamma$  is the tilt of the dipoles away from the tangent, as described in Table S1. The circular symmetry is manifest in the two-fold degeneracy  $E_{k,\nu} = E_{-k,\nu}$  and the dipole selection rule  $\vec{D}_{k,\nu} \propto \delta_{k,\pm 1}$ , and the dimerisation



in the splitting by  $2(Q_1 - Q_2)$  of the energies into two bands, denoted by  $\nu$ .

The concentration of dipole strength in the upper and lower bands is a function of  $\Phi(1) + \gamma$ , which reflects the amount of dimerisation. Increasing dimerisation,  $Q_1 > Q_2$ , leads to  $\Phi(1) + \gamma \ll 1$  and, consequently, more dipole strength in the lower band. For the LH1, more than 97% of the total absorbing strength is in the low-lying  $|k = \pm 1, 1\rangle$ , which is responsible for the strong response of the LH1 at  $E(\pm 1, 1) \equiv 880$  nm.

The functional advantage of this dipole strength concentration becomes clear after calculating the coupling between the LH1 and  $P$ -pigments. The  $P870$  band corresponds to absorption by the state  $|P870\rangle = \frac{1}{\sqrt{2}}(|P1\rangle - |P2\rangle)$  since the dipole moments of the  $P$ -pigments are nearly anti-parallel. This bright special pair state is modeled by:

$$\vec{r}_{P870} = \begin{pmatrix} 0 \\ 0 \end{pmatrix} \quad \vec{D}_{P870} = \sqrt{N}d \begin{pmatrix} \cos\beta \\ \sin\beta \end{pmatrix} \quad (\text{A16})$$

where  $N = 2$  and  $\beta$  parameterizes the dipole moment of  $|P1\rangle$ , approximately lying in the plane of the ring. The coupling between LH1 excitons and  $P$ -pigments, is then, after some algebra using equation A3:

$$V_{k,1} = \langle P870 | J | k, 1 \rangle = \delta_{k,\pm 1} \frac{\sqrt{MN}}{2} \frac{d^2}{R^3} \cos\left(\frac{\Phi(1) + \gamma}{2}\right) \times (\mp i) e^{\pm i(\beta - \Delta\gamma)} (1 \pm 3ie^{\pm i\Delta\gamma} \sin\Delta\gamma) \quad (\text{A17})$$

$$V_{k,2} = \langle P870 | J | k, 2 \rangle = \delta_{k,\pm 1} \frac{\sqrt{MN}}{2} \frac{d^2}{R^3} \sin\left(\frac{\Phi(1) + \gamma}{2}\right) \times (\mp i) e^{\pm i(\beta - \Delta\gamma)} (1 \pm 3ie^{\pm i\Delta\gamma} \sin\Delta\gamma), \quad (\text{A18})$$

where  $R$  is the radius of the LH1 ring. These expressions illustrate a selection rule,  $V_{k,\nu} \propto \delta_{k,\pm 1}$ , for the coupling between LH1 excitons and the  $P$ -pigments, and show that increased dimerisation enhances the coupling between  $P870$  and the near-resonant  $|\pm 1, 1\rangle$ , boosting Förster rates. Since  $|P\rangle$  only effectively couples to  $|k = \pm 1, 1\rangle$ , we need only three-levels in order to characterize RC-LH1 interactions. In what follows we drop the index  $\nu$  and consider the exciton states and their associated dipole moments:

$$|k = \pm 1\rangle = \frac{1}{\sqrt{M}} \sum_m e^{i\frac{4\pi}{M}km} (e^{i\Phi(1)/2} |m, 1\rangle - e^{-i\Phi(1)/2} |m, 2\rangle) \quad (\text{A19})$$

$$\vec{D}_{k=\pm 1} = d \sqrt{M/2} \cos\left(\frac{\Phi(1) + \gamma}{2}\right) e^{\pm i\Delta\gamma} \begin{pmatrix} \mp \frac{i}{\sqrt{2}} \\ \frac{1}{\sqrt{2}} \end{pmatrix}. \quad (\text{A20})$$

The symmetry of the problem leads to a selection rule coupling only  $|P870\rangle$  and  $|k = \pm 1\rangle$ , so the three-level Hamiltonian required to capture RC-LH1 interactions is:

$$H = \begin{pmatrix} \Delta E & V_1 & V_{-1} \\ V_1^* & 0 & 0 \\ V_{-1}^* & 0 & 0 \end{pmatrix}. \quad (\text{A21})$$

where  $\Delta E \equiv 130 \text{ cm}^{-1}$  and  $V_1 = V_{1,1}$  of equation A17. This three-level system can be reduced to an effective two-level

system by choosing a suitable basis for the degenerate  $k = \pm 1$  subspace. This basis is found to be

$$|B880\rangle = \frac{1}{\sqrt{2}} (e^{-i\psi} |k = 1\rangle + e^{i\psi} |k = -1\rangle), \quad (\text{A22})$$

$$|0\rangle = \frac{1}{\sqrt{2}} (e^{-i\psi} |k = 1\rangle - e^{i\psi} |k = -1\rangle) \quad (\text{A23})$$

where  $\psi = \arg(V_1)$ . Note that  $|\vec{D}_{B880}|^2 = \frac{M}{2}$ . In that basis the Hamiltonian becomes

$$H = \begin{pmatrix} \Delta E & V & 0 \\ V & 0 & 0 \\ 0 & 0 & 0 \end{pmatrix}, \quad (\text{A24})$$

where  $V = \sqrt{2}|V_1| \approx 13 \text{ cm}^{-1} \ll \Delta E$  using the parameters of Table S6. The effective two-level Hamiltonian in equation A24 is presented as equation 1 in the main text. Diagonalization of equation A24 leads to delocalized eigenstates

$$|P870'\rangle = \cos\theta |P870\rangle + \sin\theta |B880\rangle, \quad (\text{A25})$$

$$|B880'\rangle = -\sin\theta |P870\rangle + \cos\theta |B880\rangle, \quad (\text{A26})$$

$$\theta = \frac{1}{2} \arctan\left(\frac{2V}{\Delta E}\right). \quad (\text{A27})$$

The  $P870$  band energy does not shift to first-order in  $\frac{V}{\Delta E} \ll 1$ , but has a modified dipole strength

$$|\vec{D}'_{P870}|^2 = |\cos\theta \vec{D}_{P870} + \sin\theta \vec{D}_{B880}|^2 = |\vec{D}_{P870}|^2 \cos^2\theta + 2\Re\{\vec{D}_{P870}^* \cdot \vec{D}_{B880}\} \cos\theta \sin\theta + |\vec{D}_{B880}|^2 \sin^2\theta \quad (\text{A28})$$

$$\approx |\vec{D}_{P870}|^2 + 2\Re\{\vec{D}_{P870}^* \cdot \vec{D}_{B880}\} \left(\frac{V}{\Delta E}\right) \quad (\text{A29})$$

$$= d^2 \left( N + \frac{MN}{\sqrt{2}} \frac{d^2}{\Delta E} \cos^2\left(\frac{\Phi(1) + \gamma}{2}\right) (1 - 3\sin^2\Delta\gamma) \right). \quad (\text{A30})$$

Equation A29 is equation 2 in the main text, and equation A30 shows that the  $P870$  band increases its absorption intensity for small  $\Delta\gamma$  (dipoles nearly tangent to the ring) and  $\Phi(1) + \gamma$  (dimerized unit cell). Hence, the uphill energy landscape,  $\Delta E > 0$ , which sets transfer-to-trap as the bottleneck in the core complex, increases direct absorption in the  $P870$  band. Finally, note that, in accordance with the dipole sum rule, the  $B880$  band strength

$$|\vec{D}'_{B880}|^2 = |\vec{D}_{B880}|^2 \cos^2\theta - 2\Re\{\vec{D}_{P870}^* \cdot \vec{D}_{B880}\} \cos\theta \sin\theta + |\vec{D}_{P870}|^2 \sin^2\theta \quad (\text{A31})$$

decreases by an amount such that the total absorption intensity  $|\vec{D}'_{B880}|^2 + |\vec{D}'_{P870}|^2 + |\vec{D}_0|^2 = (M + N)d^2$  remains constant.

## b. Excitation Population Redistribution

Upon broadband excitation over the entire absorbing range, the initial state of the combined RC+LH1 system is a statistical mixture of the exciton states  $|P870'\rangle$  and  $|B880'\rangle$

weighted by their respective dipole strengths

$$\rho(0) = \frac{1}{(M+N)d^2} \left( |D'_{P870}|^2 |P870'\rangle \langle P870'| + |D'_{B880}|^2 |B880'\rangle \langle B880'| \right). \quad (\text{A32})$$

Hence, the population in the special pair is calculated, using equation A25, A26 and A28, to be

$$P_P(0) = \text{Tr} \{ \rho(0) |P\rangle \langle P| \} \quad (\text{A33})$$

$$= \frac{1}{4(M+N)d^2} \left\{ |\vec{D}_{P870}|^2 (3 + \cos 4\theta) + 2\Re \{ \vec{D}_{P870}^* \cdot \vec{D}_{B880} \} \sin 4\theta + |\vec{D}_{B880}|^2 (1 - \cos 4\theta) \right\} \quad (\text{A34})$$

where  $\text{Tr}$  is the trace operation. To explore the population redistribution in general circular aggregates and  $P$  pigment clusters, we substitute  $|\vec{D}_{B880}|^2 = \frac{M}{2}$ ,  $|\vec{D}_{P870}|^2 = N$  and  $\Delta\gamma = 0$  (which implies  $\Re \{ \vec{D}_{P870}^* \cdot \vec{D}_{B880} \} = \sqrt{\frac{MN}{2}} d^2$ ). Expanding equation A34 to second-order in  $\theta$  with this simplification gives immediately equation 3 in the main text. Increasing the number of pigments on the ring increases its radius linearly in  $M$ . The coupling between ring and RC states is then

$$V = d^2 \sqrt{\frac{MN}{2}} \left( \frac{1}{R_0 M} \right)^3 = \sqrt{MN} J \quad (\text{A35})$$

where  $R_0 = R/32$ . Fig. 4 in the main text plots the percent increase in  $P$ -population due to extended delocalization

$$\Delta P_P(0) = \frac{(P_P(0) - N/(M+N))}{N/(M+N)} \times 100 \quad (\text{A36})$$

for varying  $M$  and  $N$  using equation A34. One sees that additional  $P$ -excitation is optimized when more harvesting units surround fewer charge separation pigments,  $M > N$ . This can be understood from the second-order term in equation 3 of the main text.

### c. Inhomogeneous broadening

As discussed in Supplement A3, the physiological environment of light-harvesting complexes is highly disordered and dynamic, leading to homogeneous and inhomogeneous spectral broadening mechanisms. Our aim in this section is to show that the simple two-level model reproduces the full Monte Carlo simulations reported in Supplement A3, and gives further insight into the effects of inhomogeneous broadening. The analytical results for the modified P870 band dipole strength, P870 band energy and population redistribu-

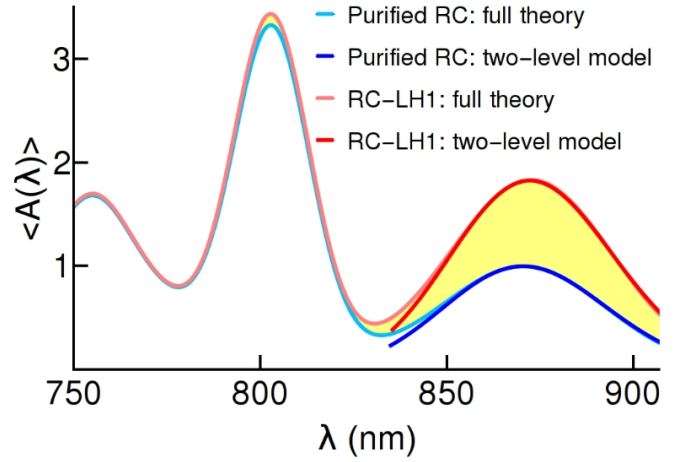


Figure 6. The full Monte Carlo simulations, detailed in Supplement A2, and the two-level model of this section make identical predictions for the isolated RC and RC-LH1 spectra. Both simulations take into account homogeneous and inhomogeneous broadening mechanisms.

tion are reproduced here

$$E'_{P870} = \frac{\Delta E}{2} + \sqrt{\left( \frac{\Delta E}{2} \right)^2 + V^2} \quad (\text{A37})$$

$$|\vec{D}'_{P870}|^2 = |\vec{D}_{P870}|^2 \cos^2 \theta + 2\Re \{ \vec{D}_{P870}^* \cdot \vec{D}_{B880} \} \cos \theta \sin \theta + |\vec{D}_{B880}|^2 \sin^2 \theta \quad (\text{A38})$$

$$P_P(0) = \frac{1}{4(M+N)d^2} \left\{ |\vec{D}_{P870}|^2 (3 + \cos 4\theta) + 2\Re \{ \vec{D}_{P870}^* \cdot \vec{D}_{B880} \} \sin 4\theta + |\vec{D}_{B880}|^2 (1 - \cos 4\theta) \right\}. \quad (\text{A39})$$

Homogeneous broadening mechanisms can be taken into account by dressing stick spectra with an appropriate lineshape function. The spectrum and the population of the special pair are averaged over the inhomogeneities of both B880 and P870 energies

$$\langle A(\epsilon) \rangle = \iint dE_{P870} dE_{B880} G(E_{P870}) G(E_{B880}) \times A(\epsilon, E_{P870}, E_{B880}) \quad (\text{A40})$$

$$\langle P_P(0) \rangle = \iint dE_{P870} dE_{B880} G(E_{P870}) G(E_{B880}) P_P(0) \quad (\text{A41})$$

where

$$A(\epsilon, E_{P870}, E_{B880}) = |\vec{D}'_{P870}|^2 g(\epsilon - E'_{P870}), \quad (\text{A42})$$

is the homogeneous absorption spectrum of the P870 with a lineshape  $g(\epsilon)$ , taken to be Gaussian in this study due to better agreement with our experimental data. Note that the Gaussian distributions,  $G(\epsilon)$ , correspond to the real inhomogeneous

spectral widths. They are therefore different than the distributions of site energies used in the full numerical simulations of Supplement A 3, which are larger than the spectral widths due to exchange narrowing effects.<sup>13</sup>

Figure 6 shows how the P870 band absorption is enhanced when extended delocalization over LH1 pigments is taken into account. This prediction matches that of the full numerical model of Supplement A 3. Hence, this simplified model can be used to make further quantitative predictions. We use it now to understand the effect of inhomogeneous broadening on the excitation population redistribution. Figure 7 shows that population is redistributed from antenna to  $P$  pigments for all realistic levels of disorder up to the full spectral linewidth (with associated standard deviation  $std \sim 200\text{-}300\text{ cm}^{-1}$ ), although the inhomogeneous broadening plays a non-trivial role. Even though the full expressions are used in this calculation, the perturbative expression, equation 3 of the main text, illustrates the physical principles. The sign of  $\Delta E$  determines the direction of the redistribution:  $\Delta E > 0$  redistributes population from antenna to  $P$  pigments, and vice versa for  $\Delta E < 0$ . Hence, in situations where the inhomogeneous spectra of LH1 and  $P$  overlap, there will be realizations where dipole strength is redistributed from antenna to  $P$  pigments and vice versa, perhaps leading to a decrease in the effect on average. However, the population redistribution is largest whenever  $\Delta E \gtrsim 0$ , so there is a non-trivial interplay between small inhomogeneity, which leads to a small but positive redistribution for each realization, and large inhomogeneity, which leads to a possibly large (for realizations which are on resonance), but sometimes negative, redistribution. Interestingly, this interplay leads to a maximum population redistribution, as shown in Figure 7, when  $\sqrt{std_{LH1}^2 + std_P^2} = \Delta E/2$ , where  $\Delta E \approx 130\text{ cm}^{-1}$  is the energy difference between the P870 and B880 spectral peaks. Remarkably, the broadenings taken in Supplement A 3, which must be used to reproduce the experimental dark-minus-light spectra, satisfy this condition. Note that the inhomogeneous broadening of the RC taken here is equal in magnitude to that of RC models determined by photon-echo and hole burning experiments<sup>1</sup>. This result gives further quantitative insight into a general design principle, where environment engineering may allow one to, as nature has, exploit this noise-assisted process<sup>19</sup>.

### 3. Simulating Difference Spectra: Numerical Simulations

Illumination of the core complex induces excitation of the special pair. The excited state,  $P^*$ , initiates a chain of charge transfer steps within the RC pigments which results in the oxidation  $P \rightarrow P^+$ . After such charge separation is produced, the oxidised special pair  $P^+$  no longer has the electronic properties of  $P$ . In particular, it no longer possesses a transition associated with absorption at 870 nm. As a result, both the optical response and the coherent interactions between the P870 transition and other pigments are suppressed. Additionally, the charge separation changes the charge distribution within the entire RC, which induces several effects in the optical spectra

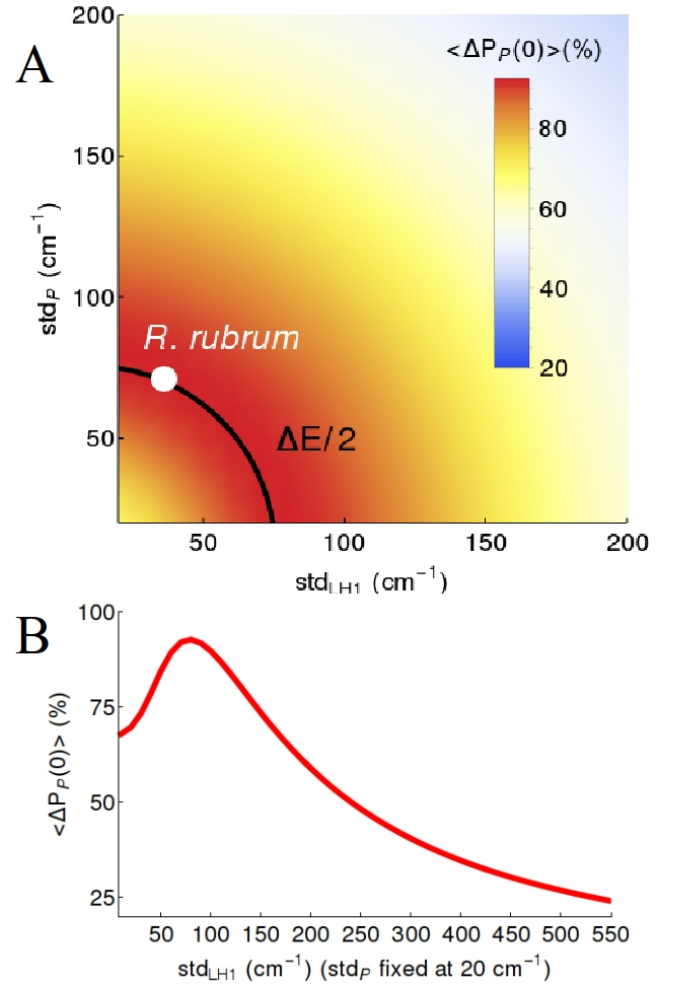


Figure 7. Averaging the change in  $P$  pigment excitation population, using equation A28, over Gaussian distributions in (A) energies of LH1 and  $P$  exciton states and (B) energy of LH1 exciton state while fixing the inhomogeneous linewidth of P870 at  $20\text{ cm}^{-1}$ . Population is always redistributed from antenna to  $P$  pigments, but the redistribution depends non-trivially on the inhomogeneous linewidths. A maximum appears when  $\sqrt{std_{LH1}^2 + std_P^2}$  is commensurate with half the energy splitting between P870 and B880.

of the B and H<sup>31</sup>. Hence, “light” spectra – recorded from samples being subject to high illumination – will not show a contribution from the P870 band while “dark” spectra – obtained from samples subject to low illumination, such that  $P^+ \rightarrow P$  occurs before the absorption of the next photon – will preserve the optical response of  $P$ . Experimentally recorded spectra and the theoretical calculation for these two situations is presented in Fig. 2A of the main text.

The positions of peaks in optical absorption spectra correspond to the energies of optically active transitions, and peak broadening arises due to the interaction of excited state degrees-of-freedom with the environment. This interaction can induce decay to the electronic ground states or can result in variation of the electric field in the neighbourhood of pigments, resulting in dynamical changes of the excited state

energies. Both mechanisms broaden the absorption lineshape, but the latter dominates in condensed matter systems. Depending on the timescale on which variations are produced, the broadening is termed homogeneous or inhomogeneous. Homogeneous broadening acts within the lifetime of electronic excitation while the inhomogeneous component leads to differences among elements in the ensemble at a given time. In this section we perform full Monte Carlo calculations to simulate the experimental difference spectra. This procedure yields very good agreement with experimentally determined difference spectra (Fig. 2 of the main text).

Physiological conditions, and the associated high temperatures, lead to rapid fluctuations of local electric fields, making the homogeneous contribution the most relevant for our analysis. Accordingly, a set of parameters has been chosen to dress stick spectra resulting from stochastic realisations of inhomogeneities,  $\sigma_e$  and  $\sigma_J$ , in the site energies and couplings, respectively, with a lineshape function such that the homogeneous contribution dominates over the inhomogeneous. The homogeneous line shape illustrates microscopic details of the interaction between pigments and the surrounding protein. Spectra are calculated by binning the histograms of dipole strength from realisations of equation A5 followed by dressing with a suitable homogeneous lineshape function, which depends on the details of the transition of interest.

The most notable differences between dark and light RC spectra of Fig. S4A, besides the disappearance of the P870 resonance, are (1) slight energy shifts and (2) an increased height of the B and H resonances at approximately 800 and 750 nm, respectively. Both changes have been previously documented<sup>14</sup> and can be taken into account theoretically by blue and red shifts of  $+33 \text{ cm}^{-1}$  and  $-39 \text{ cm}^{-1}$  in B and H energy, and a corresponding increase in the transition dipole moment  $+0.2 \text{ D}$  and  $+0.6 \text{ D}$ , respectively. The electronic RC Hamiltonian has been modified from that of *Rb. sphaeroides*<sup>25</sup> in order to match the experimentally determined absorption spectra of the RC in *R. rubrum*. Tables S2-S4 summarize parameters for the RC used in full numerical simulations. Measured and calculated absorption spectra of purified RC are shown in Fig. S4.

It is well established that, under different stages of LH1 assembly, the transition dipole strength of the B880 band, corresponding to the  $Q_y$  transition dipole moments, varies due to interactions with the  $B_x$  and  $B_y$  transition dipole moments<sup>15,16</sup>. This increases the effective  $Q_y$  transition dipole moment, and leads to a total absorption intensity in the core complex which is greater than that expected from BChl pigments in solution. This change of intensity is captured by an increased transition dipole strength for chromophores, namely, from  $6.3 \text{ D}$  to  $\approx \sqrt{2.4} 6.3 \text{ D} = 9.8 \text{ D}$ .

To calculate spectra for the core complex, interactions between RC pigments and LH1 pigments are calculated using the dipolar couplings given by equation A3. Fig. S4B shows “light” and “dark” spectra of the core complex. The theoretical and experimental curves in Fig. 2 of the main text correspond to the subtraction of “dark” minus “light” spectra in Fig. S4A and S4B. Although absorption in the core complex is delocalized across RC and LH1, one can also access numerically

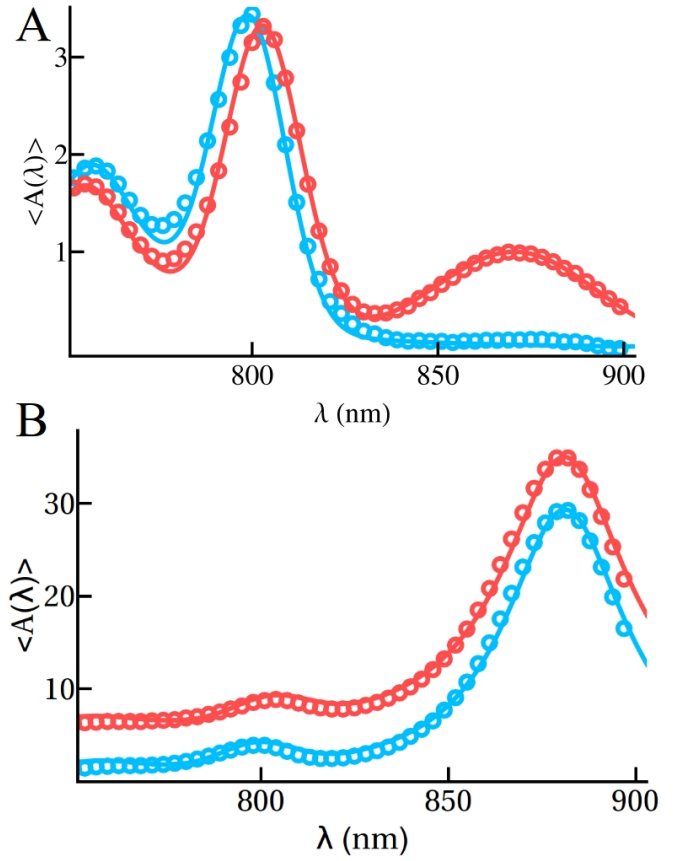


Figure 8. “Dark” and “light” spectra in red and blue, respectively. In (A) isolated RC spectra and in (B) core complex spectra. The difference spectra of (B) is Fig. 2(b) in the main text, also shown here (dark green) for clarity. The LH1 complex is responsible for the large absorption maximum at 880 nm in (B). Theory is shown in continuous and experiment is shown with circles.

the absorption spectrum of RC-like states (those states with more than 50% RC character), which shows a 78 % enhancement in absorption in the P870 region, shown in Fig. 1B of the main text. This absorption redistribution leads to a population redistribution, using equation A33. Taking into account delocalization between RC and LH1 pigments leads to an average initial excitation population in the special pair  $P_P(0) = 0.050$  as compared to  $P_P(0) = 0.028$ . Given that these numerical simulations account for all the RC pigments, they differ from those required for the initial condition of the rate model presented in Figure 3 since the latter model only accounts for the special pair in the RC.

#### a. Effect of inhomogeneous broadening

From linear spectra alone, it is difficult to discriminate contributions from inhomogeneous and homogeneous broadening mechanisms. For the RC we chose a set of parameters for diagonal and non-diagonal noise, such that the standard deviation of the P870 resonance is about  $\sim 70 \text{ cm}^{-1}$ . A study



which combined hole burning and photon echo experiments to estimate the homogeneous contribution<sup>1</sup> found, from careful analysis of pump-probe data, a standard deviation in the P865 of *Rb. sphaeroides* (analogous to P870 in *R. rubrum*) of 73 cm<sup>-1</sup>. For the ring structure, 2D non-linear spectroscopy has provided evidence, due to the circular line-shapes observed in the rephasing direction of diagonal peaks at room temperature, of a major contribution of homogeneous broadening mechanisms in the LH2 aggregates<sup>17</sup>. LH2 complexes have often been used as analogue structures of LH1 for structural analysis. The absence of wavelength dependence in room-temperature fluorescence of *R. rubrum* also implies a dominant homogeneous broadening mechanism<sup>32</sup>. However, beyond the fact that homogeneous broadening is dominant, exact numbers for each of the broadening mechanisms are hard to read out from these experiments. Moreover, measurements performed at lower temperatures present major contributions from inhomogeneous broadening<sup>32</sup>. Here we study the robustness of the dipole redistribution for different degrees of inhomogeneous noise in order to clarify their non-trivial effects.

Figure 9 presents the enhancement of the P870 resonance due to the coherent coupling with ring pigments for different levels of inhomogeneities in the intra-ring couplings, i.e. the non-diagonal Hamiltonian elements, while keeping the diagonal disorder fixed. Off-diagonal disorder has been shown to be crucial to explain fluorescence anisotropy<sup>4</sup>. For comparison, this Figure also shows the isolated RC spectra obtained experimentally. In each case the isolated RC spectrum calculated numerically is fitted to the experiment by tuning the homogeneous broadening. This study reinforces the findings of Supplement A 2 c. That is, the dipole strength redistribution is qualitatively robust to inhomogeneous broadening, and the redistribution is maximized for intermediate levels of disorder.

#### 4. Generalization to other geometries in purple bacteria species

The closed-ring circular symmetry of *R. rubrum* seems to be robust in that species<sup>7</sup>; however, different geometries have been observed in other species. For instance, there is good evidence, from high-resolution atomic force spectroscopy, as well as cryoelectron spectroscopy, that the LH1 ring of the PSU from *Rb. sphaeroides* is interrupted by other protein subunits, corroborated by biochemical evidence that only 24 BChls are present in the LH1 structure<sup>18</sup>. More recently, the structure of *T. tepidum*, the highest-resolution structure yet obtained, has provided evidence of an oval-shaped LH1 with an eccentricity of 0.4<sup>10</sup>. We have performed detailed numerical simulations for structural perturbations such as these in order to prove the robustness of the RC cross-section enhancement *in situ*, as compared to the isolated forms.

We perform Monte Carlo simulations of *Rb. sphaeroides* with parameters based on previous agreement between simulated and measured spectra<sup>18,25</sup>. In our analysis we use the structure of Ref.<sup>19</sup>, the LH1 parameters from Ref.<sup>4</sup> and tune the site energies to obtain an LH1 absorption spectra

which peaks at 875 nm, as observed experimentally. The IR resonances in *Rb. sphaeroides* have been measured to vary between 870 and 875 nm, depending on the reconstitution process<sup>20,21</sup>. We develop calculations based on the ring resonance peaking at 875 nm<sup>21</sup>. Hamiltonian and noise parameters from the RC of *Rb. sphaeroides* are taken from<sup>25</sup> while RC homogeneous broadening parameters are presented in Table S5. As a check on parameters, spectra of RC and LH1 for this species are calculated and presented in Fig. 10; they are qualitatively similar to previous work<sup>25</sup>, and most importantly, the anti-symmetric *P* band and the LH1 band peak around 865 and 875 nm, respectively.

In a first set of simulations, the complete 16 $\alpha\beta$  circular LH1 aggregate is investigated. Figure 10(A) shows the enhancement in the absorption strength of the *P* band due to the coherent interaction with the LH1 pigments. The enhancement is less than that observed in *R. rubrum* because, here, the LH1 dipole moment is smaller. This leads to a reduced coherent coupling and dipole redistribution according to equation A30. As noted earlier, hyperchromism in *R. rubrum* leads to intensity borrowing of the *Q<sub>y</sub>* band<sup>15</sup>. Such an effect has not yet been studied in any other species, and hence cannot be generalised or disregarded. Accordingly, an exact value for the dipole strength associated with the *Q<sub>y</sub>* transition dipole of pigments in other species is hard to obtain; values of 6.1, 7.7 and 11 D have been reported<sup>22–24</sup>. Hence, for these simulations 6.3 D (dashed), corresponding to the bare transition dipole of BChla, and 9.8 D (dotted), corresponding to the measured hyperchromism of *R. rubrum*, are used in Figure 10(A). With 6.3 D the increase of the RC cross-section is 17 %, while 9.8 D yields a 75 % increase.

The second set of simulations takes into account more recent structural information that displays an LH1 complex arranged on an arc with 14  $\alpha\beta$  units, corresponding to 28 pigments. For comparison purposes, the parameters of the 16-fold symmetric case are used. The absorption spectra of the LH1 complex for the 16-fold symmetric and 14-dimer rings are presented in Figure 10(B). The missing dimer structure, shown in the inset, produces a spectrum which is slightly wider than that of the complete circular aggregate. Hence, in order to compare changes in the RC spectrum we reduce the inhomogeneous broadening to  $\sigma_J = 30$  cm<sup>-1</sup> in the 14-dimer case such that its corresponding spectrum is as wide as that from the 16-fold symmetric structure. In addition, no hyperchromism is posited, so that the bare dipole moment,  $d = 6.3$  D, is used. Figure 10(C) shows the enhancement in the absorption strength of the *P* band due to the coherent interaction with the LH1 pigments. Note that the enhancement in the 16-fold symmetric case is greater than that of the 14-dimer case. As shown in equation A30, the magnitude of the dipole strength enhancement depends linearly on the number of dipoles in the special pair and LH1 ring,  $N$  and  $M$ , respectively. It is therefore natural to expect a smaller enhancement with  $N = 2$ ,  $M = 28$  as opposed to  $N = 2$ ,  $M = 32$ . To avoid this pigment number effect and investigate the effect of microscopic details of the structure, Figure 10(D) compares RC-like spectra of the 16-fold symmetric ring and the 14-dimer ring when the transition dipole of the latter is increased from

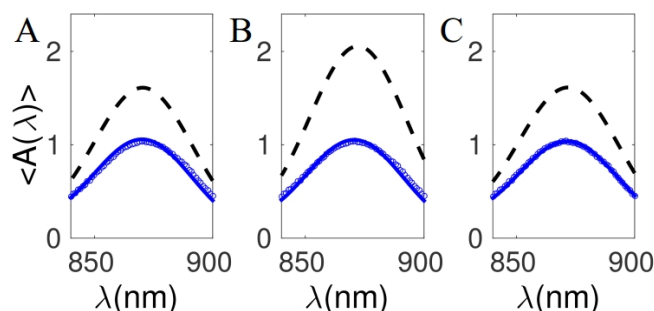


Figure 9. The effect of inhomogeneous broadening in the P870 band. In all plots experimental “dark” spectra for isolated RC are represented with circles; they are almost indistinguishable from numerical calculations for isolated RC (solid blue lines). In black are shown the spectra of RC-like states, i.e. states with an excitation population of more than 50% in the RC. In A, B and C the standard deviations of both nearest-neighbour ring couplings and *P* pigments energies, are 20, 100 and 200  $\text{cm}^{-1}$ , respectively. These figures show that the dipole strength redistribution is qualitatively robust to noise and maximized for intermediate levels of disorder.

6.3 D to  $6.3 \times 32/28$  D. As apparent from Figure 10(D), this consideration explains most of the difference between the two spectra. In order to understand why the curves do not overlap, further comment is required.

In general, perturbations from a perfect ring lead to a redistribution of transition dipoles in the ring, to other levels different than  $k = \pm 1$ . In the case of the missing dimers, the  $k = 0$  level gains dipole strength at the expense of a concomitant reduction in the  $k = \pm 1$  band. Given that  $k = 0$  level is further off-resonance than the  $k = \pm 1$  from the P870 band, its dipole strength does not appreciably increase the RC cross section.

A preliminary investigation of oval perturbations shows similar results to Figure 10. Oval-like structures have been reported for the PSUs of the purple bacteria *T. tepidum* and *Rps. palustris*<sup>10,30</sup>. We have observed that the quantitative enhancement can be closely related to the dipole strength distribution in the LH1 manifold, itself dependent on the geometrical configuration.

This study shows that a proper quantification of the dipole strength redistribution, from antenna to *P* pigments, can give insight into the fine details of the couplings, energy landscape and ring geometry. However, the most important finding of these examples is that we always find an increase in the RC cross-section due to the coherent interaction with the symmetric or the slightly-perturbed ring, which supports the assertion of generality across purple bacteria core complexes.

## 5. Methods for determination of the RC-P870 contribution after oxidation of the intact, membrane embedded PSU with stoichiometric amounts of $\text{K}_3\text{Fe}(\text{CN})_6$

### a. Diagnostic features of the RC redox spectrum

It is now well-accepted that the oxidation of the purified RC with small amounts of a strong oxidizing agent, such as  $\text{K}_3\text{Fe}(\text{CN})_6$ , leads to spectral changes in the near-IR region which correspond perfectly to those observed after photobleaching with actinic light. A typical example, obtained by the  $\text{K}_3\text{Fe}(\text{CN})_6$ -induced oxidation of the purified RC (in

detergent solution) from *R. rubrum* is shown in Fig. S7A. Under these conditions of oxidation the P870 band is essentially abolished, and the 803 nm peak, corresponding to the accessory BChl is slightly increased in intensity and blue-shifted. It has been shown previously<sup>1</sup> that the absorption transitions contributing to P870 are in fact split upon oxidation to P870+, with one component being shifted to about 800 nm (hence the observed changes to the 803 nm peak) and the other to 1260 nm (which is not visible with our instrumentation). For diagnostic purposes with real biological preparations, the redox difference (reduced RC - oxidized RC) spectrum (Fig. S7B) is a more reliable indicator of RC activity, since any contributions due to inactive RC are cancelled out.

A very useful feature of the RC redox spectrum is the crossover point and relative intensities of the flanking regions (indicated by a dotted line in Fig. S7B) at the 803 nm region. *This feature is uniquely due to RC oxidation*, and is not observed from isolated LH1s subject to oxidation. In a complex mixture, therefore, this feature can be used as a diagnostic feature to distinguish RC and LH1 contributions, respectively.

### b. Measurement conditions for obtaining spectra of purified RCs and chromatophores

Chromatophores (intracytoplasmic membranes containing the PSUs and reaction centers) were isolated from anaerobic, phototrophic cultures of *R. rubrum* S1 as described<sup>14,15,25</sup>. Absorbance spectra of 500  $\mu\text{l}$  samples (chromatophores: diluted in 20 mM TrisHCl, pH 8.0 (20T8)) were usually measured at room temperature in 2 mm path-length cuvettes with a Jasco V-560 UV/VIS spectrophotometer equipped with a near-IR-sensitive photodiode detector for turbid samples (slit width 2 nm, scanning speed 200 nm/min, photomultiplier response fast). Purified RCs (purified by a slightly modified method of Vadebonceur *et al.*<sup>14</sup>, were diluted in 20 mM TrisHCl, pH 7.7 containing 50 mM NaCl and 0.05 % (w/v) dodecyl- $\beta$ -D-maltoside, prior to measurement. For routine chemical oxidation of isolated RCs (A870 (2 mm path-length) = 0.016), a few grains of potassium ferricyanide ( $\text{K}_3\text{Fe}(\text{CN})_6$ ) were added directly to the cuvette prior to measurement.

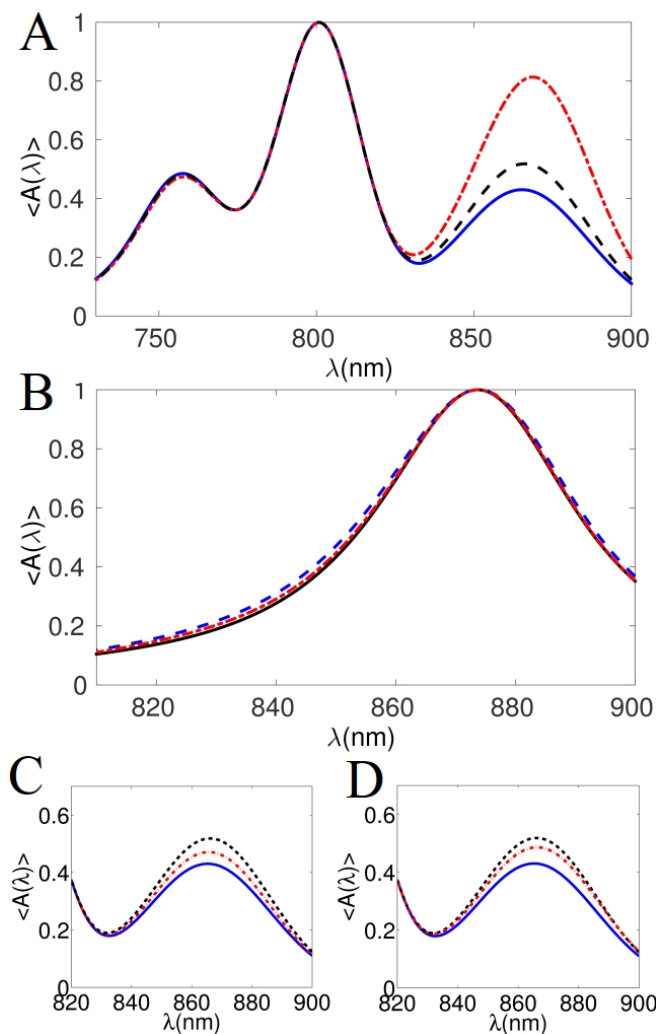


Figure 10. The effect of breaking the 16-fold ring symmetry on the dipole redistribution. Figure (A) shows the RC (continuous) and RC-like for hyperchromic ( $d = 9.8$  D) (dot-dashed) and non-hyperchromic ( $d = 6.3$  D) (dashed) spectra in the 16-fold symmetric LH1 structure. Figure (B) compares the LH1-like spectra (spectrum of states with more than 50% excitation population in the LH1 pigments) for the 16-fold symmetric (continuous) and 14-dimer (dashed) structures using the same amount of inhomogeneous noise. Over the 16-fold symmetric curve lies a 14-dimer absorption spectra (dot-dashed) with reduced inhomogeneous width. In (C) a comparison between RC-like states of the 16-fold symmetric structure (dashed) and 14-dimer structure with reduced inhomogeneity (dotted-dashed). In (D) the same comparison is shown, but the dipole strength in the LH1 for the 14-dimer case is 7.2 D instead of 6.3 D to account for the effect of the missing pigments. Most importantly, one sees an appreciable increase in the dipole strength of the  $P$  pigments when extended delocalization is taken into account.

### c. Determination of the RC concentration from a spectrum obtained from total chromatophores

A precise determination of the RC concentrations is an essential prerequisite for stoichiometric oxidation. In princi-

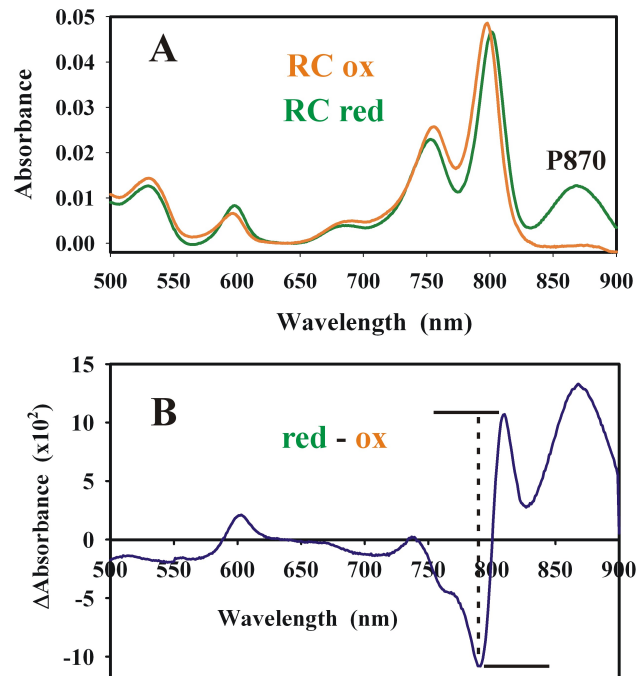


Figure 11. (A) Absorption spectra of reduced and oxidized RC, respectively. The position of the special pair (P870, Gaussian fit:  $\lambda_{max} = 869$  nm,  $\sigma = 19.6$  nm) is indicated. (B) Redox (reduced RC - oxidized RC) difference spectrum. The position and intensity of the 803 nm crossover, used as a reference point for fitting, is indicated.

ple, the RC concentration in total *R. rubrum* chromatophores might be determined from the 803 nm peak, which is exclusively due to the RC-accessory BChl. Unfortunately, the 881 nm peak of the LH1 exhibits significant intensity in the flanking region at 803 nm (see Fig. S8), which makes the assignment of the baseline solely due to the RC 803 nm peak difficult. To solve this problem unambiguously, we compared the spectrum from the wild-type (LH1+RC) with that of a RC-minus mutant, SKΔLM, where the L- and M subunits of the RC have been deleted (described in Ref.<sup>26</sup>). We have previously shown that the absorption spectra and also ultrafast transfer times for energy transfer amongst BChl and carotenoid pigments of the LH1 of the mutant are unchanged when compared with those of the wild-type LH1<sup>26</sup>. We then fitted the SKΔLM spectrum to the wild-type spectrum, using the criterium that the right flanking region, between 882 - 900 nm, is due solely to the contribution from the LH1. This fit (see Fig. S8, expanded insert) enabled us to set a reference point for the position of the RC baseline. We note that the SKΔLM fitted spectrum now corresponded perfectly to the position of the LH1  $Q_x$  band at 589 nm (data not shown). This calculation showed that for the LH1+RC chromatophores, about 48% of the intensity at 803 nm arises from the RC accessory BChl. Using the millimolar extinction coefficient of  $\epsilon(803 \text{ nm}) = 329 \text{ mM}^{-1} \cdot \text{cm}^{-1}$ <sup>14</sup>, we calculated that 243 nmol

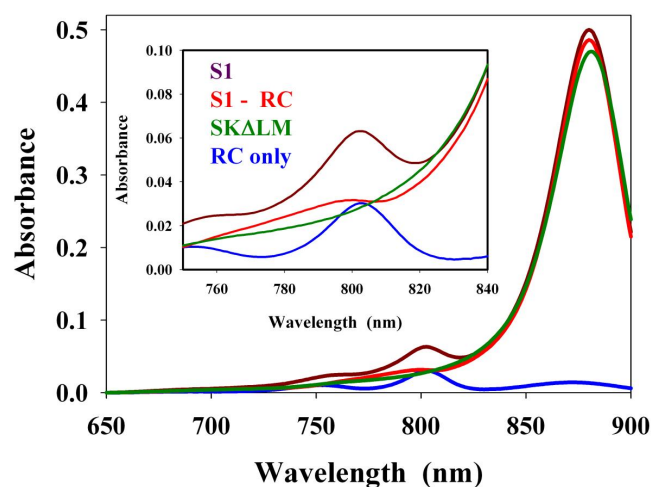


Figure 12. Absorption spectra used for the determination of the RC content. The effective RC baseline was determined from the difference in intensity at 803 nm from spectra of isolated chromatophores from the wild-type S1 (LH1 + RC, brown line) and a RC- mutant SKΔLM (LH1 only, green line). The calculated RC spectrum (using the spectrum obtained from purified RC (see Fig. S7A) is shown in blue. The spectrum shown in red corresponds to the (LH1+RC) chromatophores *minus* the calculated, purified RC spectrum.

RC are present in the cuvette under the conditions used.

#### d. Stoichiometric oxidation of the RC with $K_3Fe(CN)_6$

For a precise titration of the RC special pair redox state in chromatophores (A881 (2 mm path-length) = 0.37), incremental amounts of  $K_3Fe(CN)_6$  (0 - 560 nmol (stock solution 20 mM  $K_3Fe(CN)_6$  solution (in  $H_2O$ ))) were added to a chromatophore suspension, containing approximately 243 nmol RC, as calculated from the extinction at 803 nm. Generally, the chromatophores were incubated with redox agent at 25°C for 5 min prior to measurement in the Jasco spectrophotometer, as described above. Prior to quantitative analysis, the spectra were normalized to the baseline intensity at 640 nm, where no absorption due to pigment occurs.

The results of a typical redox titration are shown in Fig. S9A. We observed, that *even at stoichiometric levels of  $K_3Fe(CN)_6$  to RC*, that the 882 nm peak due to the LH1  $Q_y$  absorption maximum is also reduced (note that this bleaching corresponds to *chemical oxidation* of the LH1 BChl), and this reduction is concomitant with that of the special pair oxidation. To our knowledge, this is the first time that the effects of stoichiometric oxidation upon the LH1 complex have been reported.

To proceed further, we made the initial assumption, that at higher, but still near stoichiometric quantities of  $K_3Fe(CN)_6$ , that the oxidation of the LH1 BChls (measured as the reduction of peak height at 881 nm) should be linear, whereas that of the RC (measured at 803 nm) should be constant. This can be most easily visualized by calculating the difference spec-

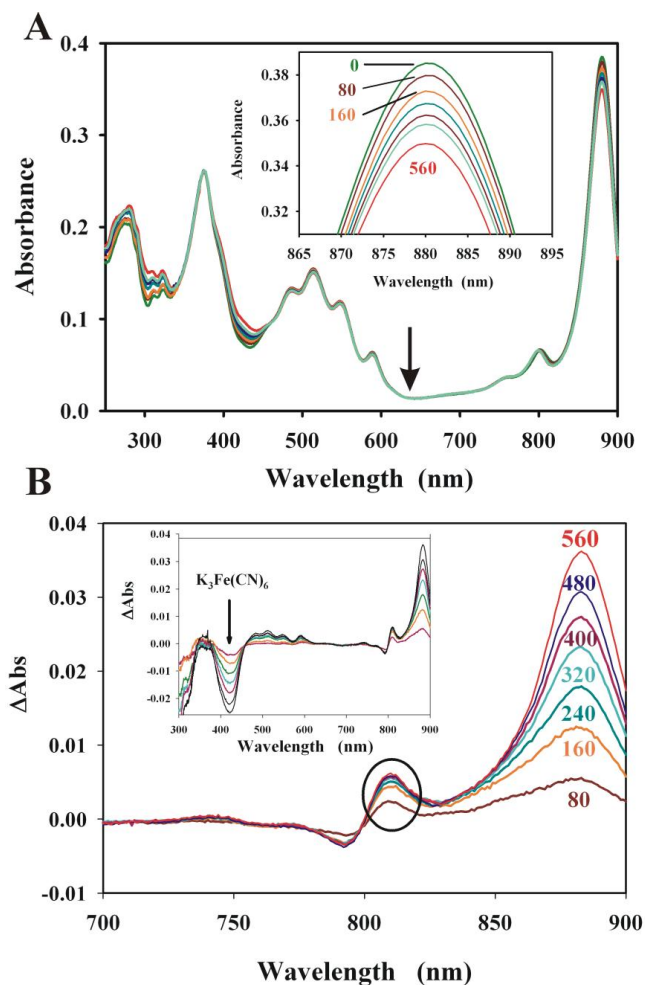


Figure 13. Reduction of the near-IR (LH1+RC) peak intensity following stoichiometric additions of  $K_3Fe(CN)_6$ . (A) The primary spectral data, obtained from chromatophores equilibrated with different concentrations of  $K_3Fe(CN)_6$  (given in nmoles). The initial data set was normalized to the intensity at 640 nm, where no absorption due to pigment occurs. Inset: enlarged near-IR region of the spectrum. (B) First near-IR difference spectra ( $\Delta Abs$ ), obtained from the data shown in (A). Each spectrum corresponds to the difference between the spectrum obtained at a given amount of  $K_3Fe(CN)_6$  (indicated) minus the reference spectrum (taken in the absence of  $K_3Fe(CN)_6$ ). Inset: the spectral difference obtained over the complete range. Note that the absorption change due to  $K_3Fe(CN)_6$  is easily visible (arrow), and can be used for control purposes.

trum (A881 (0 mM  $K_3Fe(CN)_6$ ) - A881 (x mM  $K_3Fe(CN)_6$ ) = ( $\Delta Abs_{881}$ )). The spectral results, shown in Fig S9B, confirm our hypothesis: above about 240 nmol  $K_3Fe(CN)_6$ , no further change in the 803 nm peak is observed with increasing oxidizing agent, but the A881 nm peak is incrementally reduced further. The inset in Fig. S9B also shows that no spurious effects to turbidity changes arise during this process. Quantitative analysis of these data (Fig. S10A and B) confirm the linearity of LH1 oxidation at  $K_3Fe(CN)_6$  levels where the RC is completely oxidized (Fig. S10A). The usable range for further analysis, where the RC oxidation is constant (Fig. S10B)



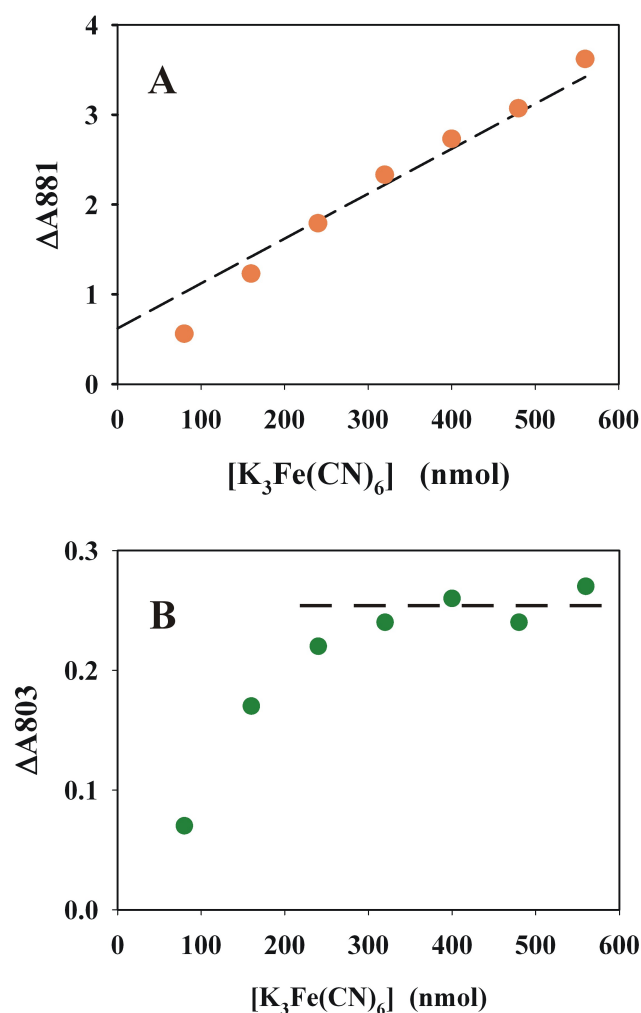


Figure 14. Variation of the peak amplitudes of the peak intensities at 881 nm (A) and 803 nm (B) respectively, obtained from the difference spectra shown in Fig. S9B. In (A) the dashed line was determined by linear regression, using the last four points (320 - 560 nmol) as input data. However, inclusion of the data point at 240 nmol had almost no effect upon the regression curve. Note that the intensities shown have been re-scaled for presentation clarity.

was shown to be between 400 - 560 nmol  $K_3Fe(CN)_6$ .

Thus, the LH1 spectral contribution present in the spectra obtained from oxidized LH1+RC chromatophores should be obtainable by subtracting pairs of difference spectra ( $\Delta Abs$ ) obtained for  $K_3Fe(CN)_6$  amounts between 400-560 nmol. In principle, any of the pairs might be employed for this purpose, but we have found it convenient to obtain a series of difference-difference spectra by subtracting sequential pairs (i.e.  $\Delta Abs_{320}-\Delta Abs_{400}$ ,  $\Delta Abs_{400}-\Delta Abs_{480}$ ,  $\Delta Abs_{480}-\Delta Abs_{560}$ ). With this series in hand (Fig. S11A), we need to perform one final control to prove that each member of this series corresponds to the same spectral form. This is done by a simple transformation. First, each (now noisy)  $\Delta\Delta Abs$  spectrum is normalized to the same maximal intensity (Fig. S11B). If the normalized spectra correspond to the same spec-

tral form, then a plot of  $\Delta\Delta Abs$  values for each pair should fall upon the same straight line. Fig. S11C shows that this expectation is fulfilled. Therefore, we can now employ the parameters of the derived LH1 spectral difference for determining the contribution in the redox spectrum obtained from the lowest amounts of  $K_3Fe(CN)_6$ , where the contribution from RC and LH1, respectively are comparable.

The final deconvolution was performed as follows. We chose to use the primary difference spectrum  $\Delta Abs(160)$  for the analysis, since visual inspection suggested significant spectral contributions from both LH1 and RC to be present. The procedure was as follows. Initially, the secondary difference spectrum  $\Delta\Delta Abs(560-480 \text{ nmol})$  (see Fig. S11A) was fitted to the spectrum  $\Delta Abs(160)$ , using the constraint that the least-squares difference *at the far red flank* (which arises almost exclusively due to the LH1 component) must be minimized. The result,  $\Delta Abs(160) - \Delta\Delta Abs(560-480 \text{ nmol})$ , is shown in green in Fig. S12A and B, and the fitted LH1 component is shown as a dashed cyan line in Fig. S12A. Also shown is a Gaussian fit ( $\lambda_{max} = 868 \text{ nm}$ ,  $\sigma = 19.6 \text{ nm}$ ) to the “P870” peak of the final spectrum, which is thus 1 nm blue-shifted compared to that obtained for the purified RC in solution (shown as the orange dashed line in Fig. S12B). In Fig. S12A, another secondary difference spectral component ( $\Delta\Delta Abs(320-240 \text{ nmol})$  is also shown (brown dashed line)). The same fitting as above, repeated using this latter spectral component, led to an identical result (not shown). In the main text, the spectrum shown in Fig. 2A has been calculated using the difference  $\Delta Abs(160)-\Delta\Delta Abs(320-160 \text{ nmol})$ . The final result however, is essentially identical to that shown in Fig. S12A,B.

### e. Methods for core complex photobleaching

The measurement of RC photobleaching was performed by comparing the “dark” spectrum obtained from total chromatophores ( $A_{881} (2 \text{ mm path-length}) = 1.06$ ) to that obtained during illumination with actinic light (using a 150 W halogen lamp). The actinic light was filtered through 3 cm of a 1 M  $CuSO_4$  solution. The amount of light quanta reaching the cuvette during illumination in this experiment was  $40 \text{ nmol cm}^{-2} \cdot \text{s}^{-1}$  (or 14000 Lux). In the dark-light experiments, the internal photomultiplier of the Jasco spectrophotometer was used instead of the photodiode, because it could be protected more easily from any stray actinic light by a long-pass filter (Asahi, XVL 0610, 1.5 mm) and a self-built chamber of black cardboard. To improve the signal-to-noise-ratio, the scanning speed was reduced to 100 nm/min, and the response was set to *slow*. In this experiment, the contribution to LH1 fluorescence was negligible. This was confirmed by performing control experiments using an Avantes diode array spectrophotometer, where the intensity of the measuring beam was sufficient to induce measurable LH1 fluorescence.

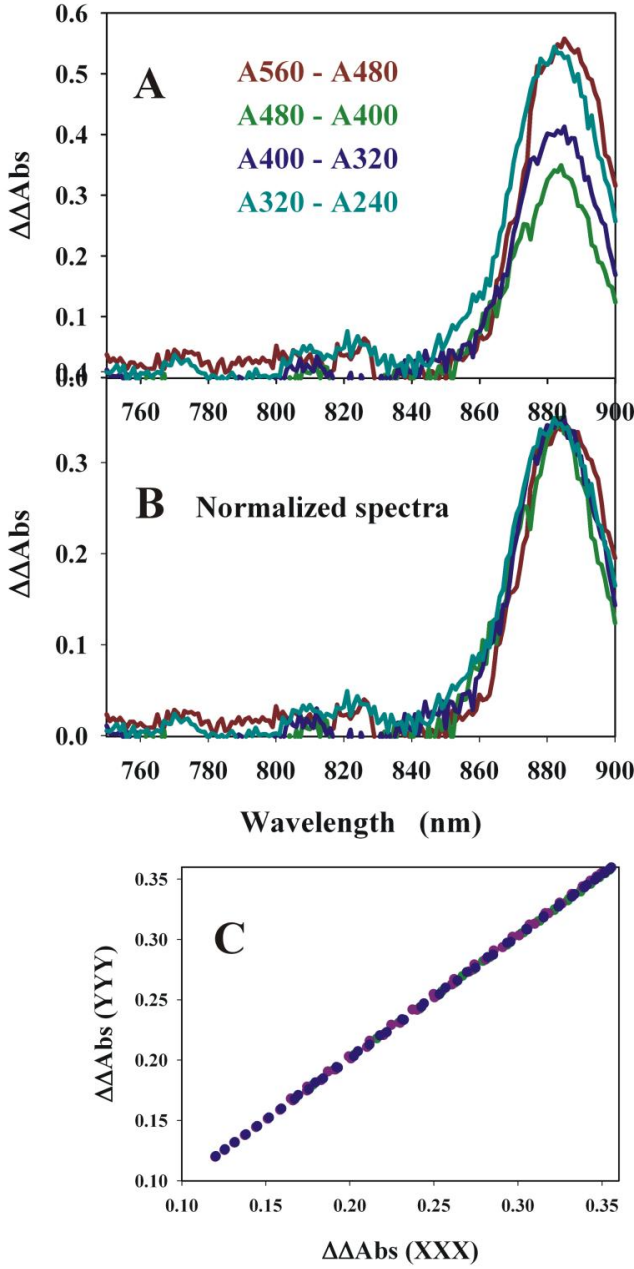


Figure 15. (A) The secondary difference spectra, obtained from the data shown in Fig. S9B. Each spectrum corresponds to the difference taken from two sequential pairs e.g.  $\Delta\Delta\text{Abs}(560-480) = \Delta\text{Abs}(560) - \Delta\text{Abs}(480)$ . (B) The difference spectra in (A) normalized to the same intensity value at 881 nm. (C) Correlation plot of the  $\Delta\Delta\text{Abs}$  intensities from sequential spectral pairs (e.g.  $\Delta\Delta\text{Abs}(560-480)$  vs.  $\Delta\Delta\text{Abs}(480-400)$ ). The intensities shown have been re-scaled ( $\times 10^2$ ) for presentation clarity. Only the intensity range corresponding to the wavelength range 800 - 900 nm has been plotted.

## 6. Charge Separation Dynamics

Excitonic transfer between the RC and LH1 occurs via a Coulomb exchange mechanism on a picosecond time-scale<sup>27</sup>, while vibrational dephasing destroys coherences in hundreds

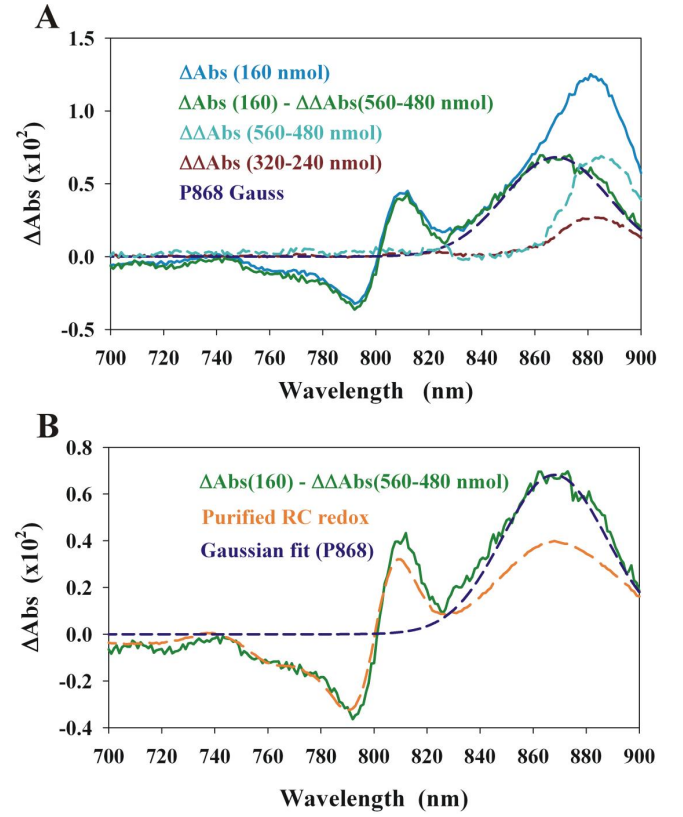


Figure 16. Deconvolution of the primary difference ( $\Delta\text{Abs}$ ) spectra into LH1 and RC components. (A) The primary difference spectrum  $\Delta\text{Abs}(160)$  (blue line), obtained at 160 nmol  $\text{K}_3\text{Fe}(\text{CN})_6$ , which contains about equal intensities from both LH1 and RC, was used for analysis. The fitting procedure was performed using the secondary difference spectrum  $\Delta\Delta\text{Abs}(560-480)$  (see Fig. S11A) (see section SI (E) for details). The result,  $\Delta\text{Abs}(160) - \Delta\Delta\text{Abs}(560-480)$  nmol), is shown in green in (A) and (B), the fitted LH1 component (dashed cyan line in (A)), and a Gaussian fit ( $\lambda_{\text{max}} = 868$  nm,  $\sigma = 19.6$  nm, dark blue dashed line) to the “P870” peak of the final spectrum, which is thus 1 nm blue-shifted compared to that obtained for the purified RC in solution (shown as the orange dashed line in (B)), are also shown. In (A), another secondary difference spectral component ( $\Delta\Delta\text{Abs}(320-240)$  nmol)) is also shown (brown dashed line). The same fitting as above, repeated using another secondary difference spectral component ( $\Delta\Delta\text{Abs}(320-240)$  nmol), brown dashed line) led to an identical result (not shown). Note that the intensities shown have been re-scaled ( $\times 10^2$ ) for presentation clarity.

of femtoseconds<sup>8,28</sup>. The Coulomb interaction de-excites an initially excited electron in the donor complex while simultaneously exciting an electron in the acceptor complex. As dephasing occurs, the excited states of donor and acceptor acquire random relative phases, which inhibits quantum mechanical delocalisation.

Transfer rates measured from pump-probe experiments agree with those obtained from calculations using generalized Förster theory<sup>27</sup>. The theoretical approach to date averages transfer from different excitonic delocalized states from a donor complex, assumed to be in a canonical equilibrium of excited states, to the acceptor complex. LH1  $\rightarrow$  RC trans-

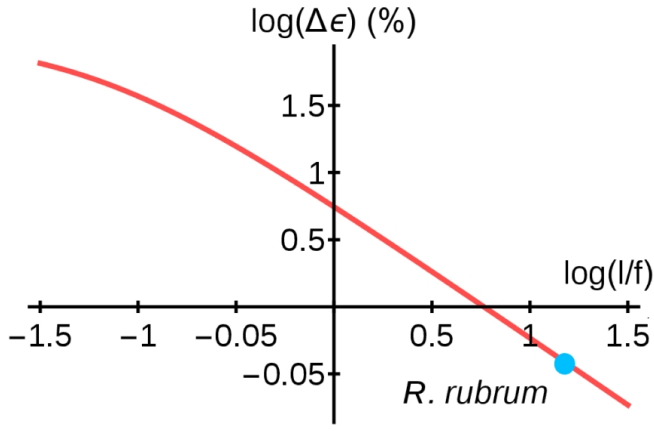


Figure 17. Increase in efficiency due to quantum delocalization as a function of the relevant incoherent transfer rates,  $l$  and  $f$ , according to equation A46. Since transfer between light-harvesting units occurs much more quickly than excitation loss ( $l/f \sim 6$ ), the increase in efficiency is small for *R. rubrum*. However, this plot illustrates that this design principle could lead to higher increases in efficiency in artificial systems like quantum dots and, in general, when the system is limited by loss ( $l/f < 1$ ).

fer occurs through the second and third lowest exciton lying states, giving rates in agreement with an experimentally measured transfer time of  $f = 40$  ps<sup>29,30</sup>. Back transfer from RC to LH1 occurs in a calculated time of  $b = 8.1$  ps<sup>31</sup>, close to the experimentally measured 7-9 ps, which was estimated from decay kinetics after RC excitation<sup>32</sup>, and further verified numerically by careful modelling of environmental effects<sup>33</sup>. The first electron transfer step,  $P^* \rightarrow P^+$ , occurs in the RC within  $c = 3$  ps<sup>34</sup>. Fluorescence, inter-system crossing, internal conversion and further dissipative mechanisms, have been included in kinetic models with a single lifetime of  $l = 250$  ps<sup>32</sup>. The rates are presented schematically in Fig. 3 of the main text.

Excitonic transfer among LH1 and RC pigments occurs in a regime where coherent delocalisation across RC and LH1 shows no appreciable effects<sup>33</sup>. Therefore, to describe excitation transfer in the core complex a model of classical rate equations taking into account LH1,  $P$ , a charge separation state  $P^+$  and a loss sink is sufficient. The system evolves according to

$$\begin{aligned}\dot{p}_{LH1} &= -\frac{1}{f} p_{LH1} + \frac{1}{b} p_P - \frac{1}{l} p_{LH1} \\ \dot{p}_P &= \frac{1}{f} p_{LH1} - \frac{1}{b} p_P - \frac{1}{c} p_P - \frac{1}{l} p_P \\ \dot{p}_{P^+} &= \frac{1}{c} p_P \\ \dot{p}_{loss} &= \frac{1}{l} (p_{LH1} + p_P).\end{aligned}\quad (A43)$$

The initial conditions

$$\begin{aligned}p_P(0) &= P_P(0) \\ p_{LH1}(0) &= 1 - p_P(0) \\ p_{P^+}(0) &= 0\end{aligned}\quad (A44)$$

for the coherent case,  $P_P(0)$  follows from equation A33, while  $P_P(0) = N/(N+M)$  when the interaction between  $P$ -pigments and the LH1 is neglected. These equations can be solved analytically for the probability of charge separation at long times:

$$p_{P^+}(t \rightarrow \infty) = bl \left( \frac{l + f P_P(0)}{c f l + b(c + l)(f + l)} \right). \quad (A45)$$

We are interested in the increase of charge separation due to extended delocalization, which changes the initial condition  $P_P(0)$ . Defining  $\delta$  to be the initial population in the  $P$ -pigments without extended delocalization, and  $\tilde{\delta} > \delta$  with extended delocalization, the percent increase in charge separation, which is the change in efficiency  $\Delta\epsilon$ , is given by:

$$\Delta\epsilon = \frac{f(\tilde{\delta} - \delta)}{l + f\delta} \quad (A46)$$

As shown in the main text and in the SI,  $\delta = \frac{2}{34}$  and  $\tilde{\delta} \approx \frac{4}{34}$ . Figure 17 shows the increase in charge separation according to Equation A46 for variable values of  $l/f$ , the ratio of the dissipation to the forward transfer time scales, which determines the increase in efficiency. Since  $f > l$  in *R. rubrum*, charge separation is very efficient ( $\sim 83\%$ ) and the benefit from population redistribution due to extended delocalization is  $\sim 1\%$ . However, for lossy systems  $f < l$ , the benefit of extended delocalization can be very large. Figure 18 gives a concrete example of a system where the probability of charge separation increases from 0.21 to 0.33, an increase in efficiency of 54 %.

## 7. Higher Plants

Photosystem 1 (PS1) and photosystem 2 (PS2) are the main light-harvesting photounits in higher plants<sup>35</sup>. To explore the effects of extended delocalization in these systems, we examine Hamiltonians of the form

$$H = \begin{pmatrix} H_{RC} & V \\ V & H_{LH} \end{pmatrix} \quad (A47)$$

where  $H_{RC}$  is the Hamiltonian of the full RC alone and  $H_{LH}$  is the Hamiltonian of the antenna complexes. The coupling between RC and LH pigments is captured by the matrix  $V$ . In this simplified calculation, site energies are taken from the literature and couplings between pigments are calculated in the point-dipole approximation using  $d = 4.48$  D,  $\kappa = 1$  and  $d = 4.4$  D,  $\kappa = 1.5$  for PS1 and PS2, respectively<sup>36–38</sup>. Dipole moments,  $\vec{D}_i$ , are calculated along the direction connecting the  $N_B$  and  $N_D$  atoms of the porphyrin rings of each chlorophyll using the atomic coordinates taken from the X-ray structures (PDB accession codes 1JB0 and 3WU2), and rotated  $15^\circ$  towards  $N_C$  in the case of PS2<sup>11,39</sup>. Fluctuations in the pigment

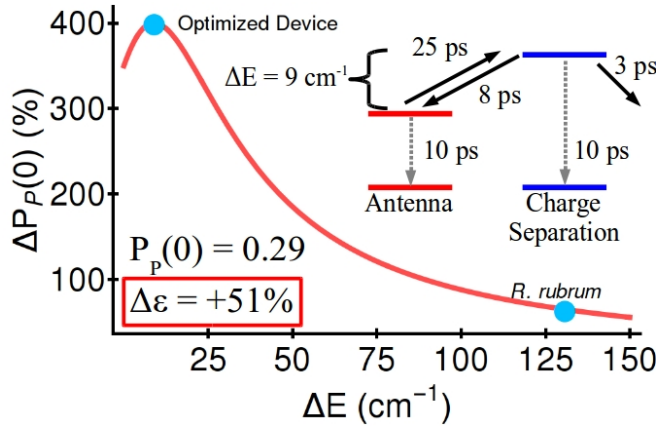


Figure 18. **Optimizing charge separation in an artificial system.** Tuning the resonance condition,  $\Delta E = 9 \text{ cm}^{-1}$ , maximizes the population redistribution ( $P_P(0) = \frac{10}{34} = 0.29$ ) according to equation A33, leading to a 400 % increase in direct excitation of the  $P$ -pigments. For a situation in which the pigments are subject to fast losses ( $f = 40 \text{ ps}$ ,  $b = 8 \text{ ps}$ ,  $c = 3 \text{ ps}$ ,  $l = 15 \text{ ps}$ ), the population redistribution increases the probability of charge separation from 0.21 to 0.33, a 54 % increase in efficiency.

energies, drawn from a Gaussian distribution, capture spectral inhomogeneities, which are known to fluctuate with temperature. We take Gaussian standard deviations of  $\sigma = 80 \text{ cm}^{-1}$  (fit from low temperature spectra) and  $\sigma = 28 \text{ cm}^{-1}$  (fit from room temperature spectra) for PS1 and PS2, respectively<sup>40,41</sup>. For each realization of the Hamiltonian,  $H$ , we find a unitary  $U$  which diagonalizes it and calculate the dipole moments of the exciton states,  $|k\rangle = \sum_i U_{i,k} |i\rangle$ , according to  $\vec{D}'_k = \sum_i U_{i,k} \vec{D}_i$ . The population in the  $P$  pigments is calculated according to:

$$\rho(0) = \frac{\sum_{\alpha} |\vec{D}'_{\alpha}|^2 |\alpha\rangle \langle \alpha|}{\sum_{\alpha} |\vec{D}'_{\alpha}|^2}, \quad (\text{A48})$$

$$\rho_P(0) = \sum_{i=1}^N \text{Tr}\{\rho(0) |P_i\rangle \langle P_i|\}. \quad (\text{A49})$$

where  $N = 2$  for PS1 and PS2 monomer and  $N = 4$  for the PS2 dimer. We compare the calculation of equation A49 for  $V = 0$  (uncoupled RC and antennae) and  $V \neq 0$  (coherently coupled RC and antennae). As summarized in figure 19, these calculations predict an increase in the excitation of  $P$  pigments due to excitonic delocalisation over antenna chlorophylls observed in the X-ray structures. Excitation redistribution from antenna to  $P$  pigments is robust to, albeit reduced by, disorder. A more sophisticated calculation, which we leave for a future work, will likely require the determination of nearest-neighbor couplings beyond the dipole-dipole approximation, which is known to break down at distances of approximately  $10 \text{ \AA}$ .

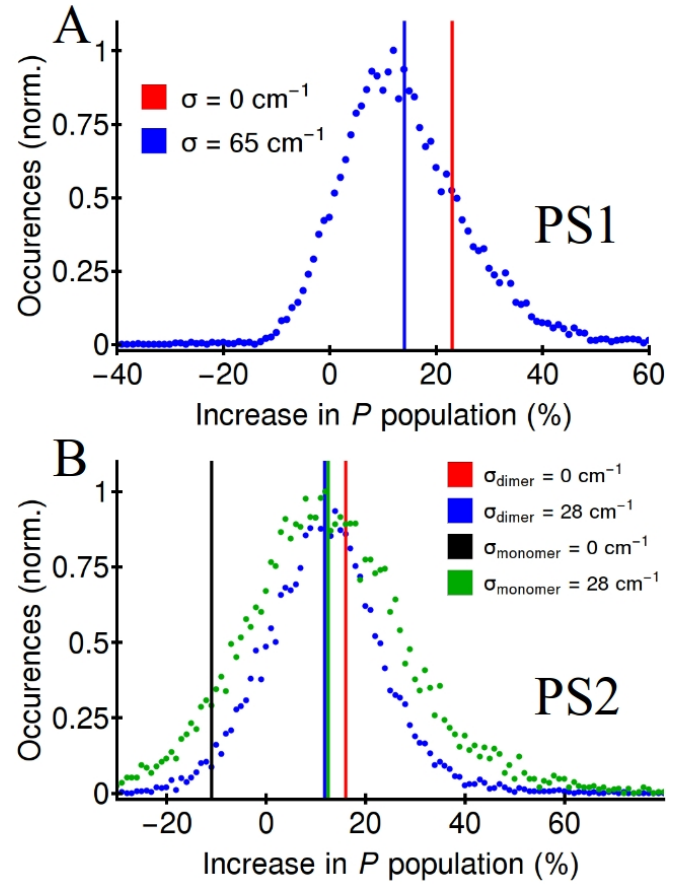


Figure 19. Excitation redistribution from antenna to  $P$  pigments in PS1 (A) and PS2 (B) is robust to Gaussian disorder in the site energies. The average change of  $P$  population in PS1 shifts from +23% with no disorder to +14% with  $80 \text{ cm}^{-1}$  inhomogeneous broadening; the distribution has a Lorentzian FWHM of 20%. In the PS2 dimer, the redistribution shifts from +16% with no disorder to +12%, Gaussian std 11%, with  $28 \text{ cm}^{-1}$  inhomogeneous broadening, and the PS2 monomer shifts from -11% to +12%, std +15%, with the same inhomogeneous broadening. Hence, although disorder levels the difference between the PS2 dimer and monomer in average, extended couplings in the dimer increase robustness to site energy fluctuations, as the distribution is narrower for the dimer.

## 8. Does quantum delocalization across photosynthetic pigments of the RC-LH1 complex contribute to evolutionary fitness?

At first glance, it would seem that an evolutionary advantage due to quantum mechanical delocalization is unlikely, as the improvement ( $\sim 1\%$ ) is small compared to the efficiency. Experimentally-derived rates yield overall efficiencies of about 85-95%<sup>33,42,43</sup>. Under our normal laboratory growth conditions, we employ light intensities of about  $24 \mu\text{E} \cdot \text{m}^{-2} \cdot \text{s}^{-1}$ , equivalent to  $1.5 \times 10^{19} \text{ photons} \cdot \text{m}^{-2} \cdot \text{s}^{-1}$ . However, the comfortable laboratory conditions do not resemble the natural ecological niche of *R. rubrum*, and only in the latter has evolutionary pressure molded the presently observable (LH1+RC) PSU structural organization. *R. rubrum* is a fresh-water bac-



terium, which is found in lakes under conditions of low light intensity and low oxygen. We can estimate the probable water depth of the ecological niche by reference to the oxygen tension which allows the expression of photosynthetic membranes. In a study by one of us (R. Ghosh<sup>44</sup>) we have shown that only under a  $pO_2$  of 0.3% are photosynthetic membranes expressed in *R. rubrum*. In a meromictic lake (where a chemical gradient between oxygen from the surface, and nutrients from the lake sediment occurs) such as Lago di Cadagno in the Swiss alps, a  $pO_2$  of 0.3% occurs at a depth of between 6 - 11 m<sup>45</sup>, depending on the season of the year. At this water depth, the light intensity may only be 1 - 0.1  $\mu E.m^{-2}.s^{-1}$ . Under these conditions, taking geometrically-determined self-shading due to the clustering of the intracellular photosynthetic membranes within the cell, the *R. rubrum* PSU must be adapted to extremely low light intensities - the incident light intensities could be as low as 60 photons.nm<sup>-2</sup>.ms<sup>-1</sup>, which may be severely limiting, considering that the time for one turnover of photoinduced cyclic electron transport is about 1 ms<sup>28</sup>. Based on these considerations, it is not unreasonable to speculate that the increase of the effective extinction coefficient of the RC due to quantum delocalization is related to the evolutionary pressure determined by the growth light intensity conditions. Finally, note that the predicted enhancement of *P*-pigment excitation in the species we studied (*R. rubrum*,  $\Delta P_P(0) = 100\%$ ; *Rb. sphaeroides*,  $\Delta P_P(0) \sim 20 - 75\%$ , depending on the hyperchromism; PS1 and PS2,  $\Delta P_P(0) = 12 - 14\%$ ) is correlated with the light intensities that these organisms experience under physiological conditions. More explicitly, lower light intensities correlate with a greater enhancement, supporting our claim that this effect could be both general and biologically relevant.

## Appendix B: Supplementary Tables

Table I. Parameters for the LH1 of *R. rubrum* which capture the absorption spectrum of Fig. S4.

Parameter	Value	Description
$\gamma$	10.06°	intra-dimer angle
$\Delta\gamma_1, \Delta\gamma_2$	19.9°, 17.6°	dipole tilt away from tangent
$\phi_1, \phi_2$	6.24°, 4.81°	dipole tilt out of membrane plane
$r_1, r_2$	46.51 Å, 47.27 Å	radius of $\alpha, \beta$ rings
$z$	0.63 Å	vertical displacement among $\alpha$ and $\beta$ chromophores
$d_{LH1}$	9.8 D	dipole moment for $Q_y$ transition of LH1
$\kappa$	2	relative permittivity
$\epsilon_\alpha, \epsilon_\beta$	12646, 12656 cm <sup>-1</sup>	chromophore energies of $\alpha$ and $\beta$ site
$Q_1, Q_2$	600, 377 cm <sup>-1</sup>	intra- and inter-dimer coupling
$\sigma_J$	60 cm <sup>-1</sup>	magnitude of nearest neighbours coupling strength disorder
$\sigma_{LH1}$	80 cm <sup>-1</sup>	magnitude of LH1 pigments energy disorder
$\Gamma_{LH1}$	36.5 nm	half width half maximum homogeneous dressing $L(\lambda, \lambda^0, \Gamma)$ for LH1 transitions

Table II. Parameters for the active RC of *R. rubrum* which capture the absorption spectrum of Fig. S4.

Parameter	Value	Description
$d_P$	6.3 D	dipole moment for $Q_y$ transition of P BChls
$d_{AP}$	6.7 D	dipole moment for $Q_y$ transition of B
$d_B$	8.2 D	dipole moment for $Q_y$ transition of H
$\sigma_P$	70 cm <sup>-1</sup>	magnitude of P pigments energy disorder
$\sigma_{AP}$	40 cm <sup>-1</sup>	magnitude of B energy disorder
$\sigma_{Bphy}$	70 cm <sup>-1</sup>	magnitude of H energy disorder
$\sigma_{VP}$	50 cm <sup>-1</sup>	magnitude of P pigments coupling disorder
$\Gamma_P$	21 nm	standard deviation homogeneous dressing for P870 transition
$\Gamma_{AP}$	9.3 nm	standard deviation homogeneous dressing for B transition at 802 nm
$\Gamma_{Bphy}$	35 nm	half width half maximum homogeneous dressing for H

Table III. Hamiltonian (in cm<sup>-1</sup> units) for the RC of *R. rubrum* in the basis  $\{|P1\rangle, |P2\rangle, |AP1\rangle, |AP2\rangle, |BPh1\rangle, |BPh2\rangle\}$ . Missing elements are calculated using equation A3.

$$\begin{pmatrix} 11990 & 500 & -60 & -70 & & \\ 500 & 11990 & -70 & -60 & & \\ -60 & -70 & 12537 & & 140 & \\ -70 & -60 & & 12537 & & 130 \\ & & 140 & & 13220 & \\ & & & 130 & & 13220 \end{pmatrix}$$

Table IV. Parameters for the oxidised RC of *R. rubrum* which capture the absorption spectrum of Fig. S4.

Parameter	Value	Description
$d_P$	0 D	dipole moment for $Q_y$ transition of P BChls
$d_{AP}$	6.9 D	dipole moment for $Q_y$ transition of B
$d_B$	8.8 D	dipole moment for $Q_y$ transition of BPh
$\epsilon_{AP}$	12 537 cm <sup>-1</sup>	B energy
$\epsilon_B$	13 220 cm <sup>-1</sup>	BPh energy

Table V. Parameters for the RC of *Rb. sphaeroides*

Parameter	Value	Description
$d_P$	6.3 D	dipole moment for $Q_y$ transition of P BChls
$d_{AP}$	6.3 D	dipole moment for $Q_y$ transition of B
$d_B$	6.3 D	dipole moment for $Q_y$ transition of H
$\sigma_P$	240 cm <sup>-1</sup>	magnitude of P pigments energy disorder
$\sigma_{AP}$	90 cm <sup>-1</sup>	magnitude of B energy disorder
$\sigma_{Bphy}$	120 cm <sup>-1</sup>	magnitude of H energy disorder
$\sigma_{V_P}$	0 cm <sup>-1</sup>	magnitude of P pigments coupling disorder
$\Gamma_P$	16 nm	standard deviation homogeneous dressing $G(\lambda, \lambda^0, \Gamma)$ for P870 transition
$\Gamma_{AP}$	11 nm	standard deviation homogeneous dressing $G(\lambda, \lambda^0, \Gamma)$ for AP transition at 802 nm
$\Gamma_{Bphy}$	25 nm	half width half maximum homogeneous dressing $L(\lambda, \lambda^0, \Gamma)$ for BPh

Table VI. Parameters for the simplified LH1 model of *R. rubrum*.

Parameter	Value
$\gamma$	10.06°
$\Delta\gamma$	$(\Delta\gamma_1 + \Delta\gamma_2)$
$R$	$(r_1 + r_2)/2$
$d$	9 D
$\kappa$	2
$\epsilon$	$(\epsilon_\alpha + \epsilon_\beta)/2$
$Q_1, Q_2$	600, 377 cm <sup>-1</sup>
$std_{LH1}^{inhom}$	36 cm <sup>-1</sup>
$std_P^{inhom}$	71 cm <sup>-1</sup>
$std_P^{hom}$	277 cm <sup>-1</sup>

## REFERENCES

- <sup>1</sup>F. Autenrieth, *The photosynthetic apparatus of Rhodospirillum rubrum: a computational approach*, Diploma thesis, University of Stuttgart (2002).
- <sup>2</sup>S. J. Jamieson, P. Wang, P. Qian, J. Y. Kirkland, M. J. Conroy, C. N. Hunter, and P. Bullough, "Projection structure of the photosynthetic reaction centre-antenna complex of *Rhodospirillum rubrum* at 8.5 Å resolution." *EMBO J.* **21**, 3927–3935 (2002).
- <sup>3</sup>J. Koepke, X. Hu, C. Muenke, K. Schulten, and H. Michael, "The crystal structure of the light-harvesting complex II (B800-850) from *Rhodospirillum rubrum*," *Structure* **4**, 581–597 (1996).
- <sup>4</sup>G. McDermott, S. M. Prince, A. A. Freer, A. M. Hawthornthwaite-Lawless, M. Z. Papiz, and R. J. Cogdell, "Crystal structure of an integral membrane light-harvesting complex from photosynthetic bacteria," *Nature* **374**, 517–521 (1995).
- <sup>5</sup>X. Hu and K. Schulten, "A model for the light-harvesting complex I (B875) of *Rhodobacter sphaeroides*," *Biophys. J.* **75**, 683–694 (1998).
- <sup>6</sup>U. Gerken, F. Jelezko, B. Götze, M. Branschädel, C. Tietz, R. Ghosh, and J. Wrachtrup, "Membrane environment reduces the accessible conformational space available to an integral membrane protein," *J. Phys. Chem. B* **107**, 338–343 (2003).
- <sup>7</sup>U. Gerken, D. Lupo, C. Tietz, J. Wrachtrup, and R. Ghosh, "Circular symmetry of the light-harvesting 1 complex from *Rhodospirillum rubrum* is not perturbed by interaction with the reaction center," *Biochemistry* **42**, 10354–10360 (2003).
- <sup>8</sup>A. Aird, J. Wrachtrup, K. Schulten, and C. Tietz, "Possible pathway for ubiquinone shuttling in *Rhodospirillum rubrum* revealed by molecular dynamics simulation," *Biophys. J.* **92**, 23–33 (2007).
- <sup>9</sup>S. Scheuring, F. Reiss-Husson, A. Engel, J.-L. Rigaud, and J.-L. Ranck, "High-resolution AFM topography of *Rubrivax gelatinosus* light-harvesting complex LH2," *EMBO J.* **20**, 3029–3035 (2001).
- <sup>10</sup>S. Niwa, L. J. Yu, K. Takeda, Y. Hirano, T. Kawakami, Z. Y. Wang-Otomo, and K. Miki, "Structure of the LH1-RC complex from *Thermochromatium tepidum* at 3.0 Å," *Nature* **508**, 228–232 (2014).
- <sup>11</sup>C. Weiss, Jr., "The  $\pi$  electron structure and absorption spectra of chlorophylls in solution," *J. Mol. Spectrosc.* **44**, 37–80 (1972).
- <sup>12</sup>A. Davydov, "The theory of molecular excitons," *Usp. Fiz. Nauk* **82**, 393–448 (1964).
- <sup>13</sup>S. Jang and R. J. Silbey, "Theory of single molecule line shapes of multi-chromophoric macromolecules," *J. Chem. Phys.* **118**, 9312–9323 (2003).
- <sup>14</sup>C. Vadeboncoeur, H. Noël, L. Poirier, Y. Cloutier, and G. Gingras, "Photoreaction centre of photosynthetic bacteria. 1. Further chemical characterization of the photoreaction centre from *Rhodospirillum rubrum*," *Biochemistry* **18**, 4301–4308 (1979).
- <sup>15</sup>R. Ghosh, H. Hauser, and R. Bachofen, "Reversible dissociation of the B873 light-harvesting complex from *Rhodospirillum rubrum* G9+," *Biochemistry* **27**, 1004–1014 (1988).
- <sup>16</sup>A. Scherz and W. W. Parson, "Exciton interactions in dimers of bacteriochlorophyll and related molecules," *Biochim. Biophys. Acta* **766**, 666–678 (1984).
- <sup>17</sup>E. Harel and G. S. Engel, "Quantum coherence spectroscopy reveals complex dynamics in bacterial light-harvesting complex 2 (Lh2)," *Proc. Natl Acad. Sci. USA* **109**, 706–711 (2012).
- <sup>18</sup>P. Qian, C. N. Hunter, and P. A. Bullough, "the 8.5 Å projection structure of the core rc-lh1-pufx dimer on *rhodobacter sphaeroides*," *J. Mol. Biol.* **349**, 948–960 (2005).
- <sup>19</sup>X. Hu and K. Schulten, "Model for the Light-Harvesting Complex I (B875) of *Rhodobacter sphaeroides*," *Biophys. J.* **75**, 683–694 (1998).
- <sup>20</sup>G. Drews, "Structure and functional organization of light-harvesting complexes and photochemical reaction centers in membranes of phototropic bacteria," *Microbiol. Revs.* **49**, 59–70 (1985).
- <sup>21</sup>S. Bradforth, R. Jimenez, F. van Mourik, R. van Grondelle, and G. Fleming, "Excitation transfer in the core light-harvesting complex (LH-1) of *Rhodobacter sphaeroides*: an ultrafast fluorescence depolarization and annihilation study," *J. Phys. Chem.* **99**, 16179–16191 (1995).
- <sup>22</sup>K. Sauer, J. R. L. Smith, and A. J. Schultz, "J. Am. Chem. Soc." **88**, 2681 (1966).
- <sup>23</sup>R. M. Pearlstein, "Photosynth. Res." **31**, 213 (1992).
- <sup>24</sup>X. Hu, T. Ritz, A. Damjanović, and K. Schulten, "Pigment organization and transfer of electronic excitation in the photosynthetic unit of purple bacteria," *J. Phys. Chem. B* **101**, 3854–3871 (1997).
- <sup>25</sup>D. Lupo and R. Ghosh, "The reaction center H subunit is not required for high levels of light-harvesting complex 1 in *Rhodospirillum rubrum* mutants," *J. Bacteriol.* **186**, 5585–5595 (2004).
- <sup>26</sup>S. Amarie, D. Lupo, M. Lenz, R. Saegesser, R. Ghosh, and J. Wachtveitl, "Excitation energy pathways in the photosynthetic units of reaction center Im- and h-subunit deletion mutants of *Rhodospirillum rubrum*," *Photosynth. Res.* **103**, 141–151 (2010).
- <sup>27</sup>X. Hu, T. Ritz, A. Damjanović, F. Autenrieth, and K. Schulten, "Photosynthetic apparatus of purple bacteria," *Q. Rev. Biophys.* **35**, 1–62 (2002).
- <sup>28</sup>H. Lee, Y. C. Cheng, and G. R. Fleming, "Coherence dynamics in photosynthesis: protein protection of excitonic coherence," *Science* **316**, 1462–1465 (2007).
- <sup>29</sup>K. Timpmann, A. Freiberg, and V. Sundström, "Energy trapping and detrapping in the photosynthetic bacterium *Rhodospseudomonas viridis*: transfer to trap limited dynamics," *Chem. Phys.* **194**, 275–283 (1995).
- <sup>30</sup>K. J. Visscher, H. Bergström, V. Sundström, C. N. Hunter, and R. van Grondelle, "Temperature dependence of energy transfer from the long wavelength antenna BChl-896 to the reaction center in *Rhodospirillum rubrum*, *Rhodobacter sphaeroides* (w.t. and M21 mutant) from 77 to 177 K, studied by picosecond absorption spectroscopy," *Photosynth. Res.* **22**, 211–217 (1989).
- <sup>31</sup>A. Damjanović, T. Ritz, and K. Schulten, "Excitation energy trapping by the reaction center of *Rhodobacter sphaeroides*," *Intl. J. Quant. Chem.* **77**, 139–151 (2000).
- <sup>32</sup>K. Timpmann, F. G. Zhang, A. Freiberg, and V. Sundström, "Detrapping of excitation energy transfer from the reaction center in the photosynthetic purple bacterium *Rhodospirillum rubrum*," *Biochim. Biophys. Acta* **1183**, 185–193 (1993).
- <sup>33</sup>J. Strümpfer, M. Séner, and K. Schulten, "How quantum coherence assists photosynthetic light-harvesting," *J. Phys. Chem. Lett.* **3**, 536–542 (2012).
- <sup>34</sup>R. G. Fleming, J. L. Martin, and J. L. Breton, "Rates of primary electron transfer in photosynthetic reaction centres and their mechanistic implications," *Nature* **333**, 190–192 (1998).
- <sup>35</sup>D. R. Ort and C. F. Yocum, eds., *Oxygenic Photosynthesis: the light reactions* (Kluwer Academic Publishers, 1996).
- <sup>36</sup>A. Damjanović, H. M. Vaswani, P. Fromme, and G. R. Fleming, "Chlorophyll excitations in photosystem I of *Synechococcus elongatus*," *J. Phys. Chem. B* **106**, 10251–10262 (2002).
- <sup>37</sup>G. Raszewski and T. Renger, "Light-harvesting in photosystem II core complexes is limited by the transfer to trap: can the core complex turn into a photoprotective mode?" *J. Am. Chem. Soc.* **130**, 4431–4446 (2008).
- <sup>38</sup>G. Raszewski, W. Saenger, and T. Renger, "Theory of optical spectra of photosystem II reaction centers: location of the triplet state and the identity of the primary electron donor," *Biophys. J.* **88**, 986–998 (2005).
- <sup>39</sup>B. Raszewski, G. Diner, E. Schlöder, and T. Renger, "Spectroscopic properties of reaction center pigments in photosystem II core complexes: revision of the multimer model," *Biophys. J.* **95**, 105–119 (2008).
- <sup>40</sup>Y. Shiwei, M. G. Dahlbom, P. J. Canfield, N. S. Hush, R. Kobayashi, and J. R. Reimers, "Assignment of the  $Q_y$  absorption spectrum of photosystem-I from *Thermosynechococcus elongatus* based on CAM-B3LYP calculations at the PW91-optimized protein structure," *J. Phys. Chem. B* **111**, 9923–9930 (2007).
- <sup>41</sup>L. Konermann and A. R. Holzwarth, "Analysis of the absorption spectrum of photosystem II reaction centers: temperature dependence, pigment assignment, and inhomogeneous broadening," *Biochemistry* **35**, 829–842 (1996).
- <sup>42</sup>T. Ritz, S. Park, and K. Schulten, "Kinetics of exciton migration and trapping in the photosynthetic unit of purple bacteria," *J. Phys. Chem. B* **105**, 8259–8267 (2001).
- <sup>43</sup>F. Caycedo-Soler, F. J. Rodríguez, L. Quiroga, and N. F. Johnson, "Light-harvesting mechanism of bacteria exploits a critical interplay between the dynamics of transport and trapping," *Phys. Rev. Lett.* **104**, 15832 (2010).
- <sup>44</sup>H. Grammel, E.-D. Gilles, and R. Ghosh, *Appl. Environ. Microbiol.* **69**, 6577–6586 (2003).
- <sup>45</sup>M. Tonolla, S. Peduzzi, D. Hahn, and R. Peduzzi, *FEMS Microbiol. Ecol.* **43**, 89–98 (2003).